Airbenders Ltd. Critical Design Report

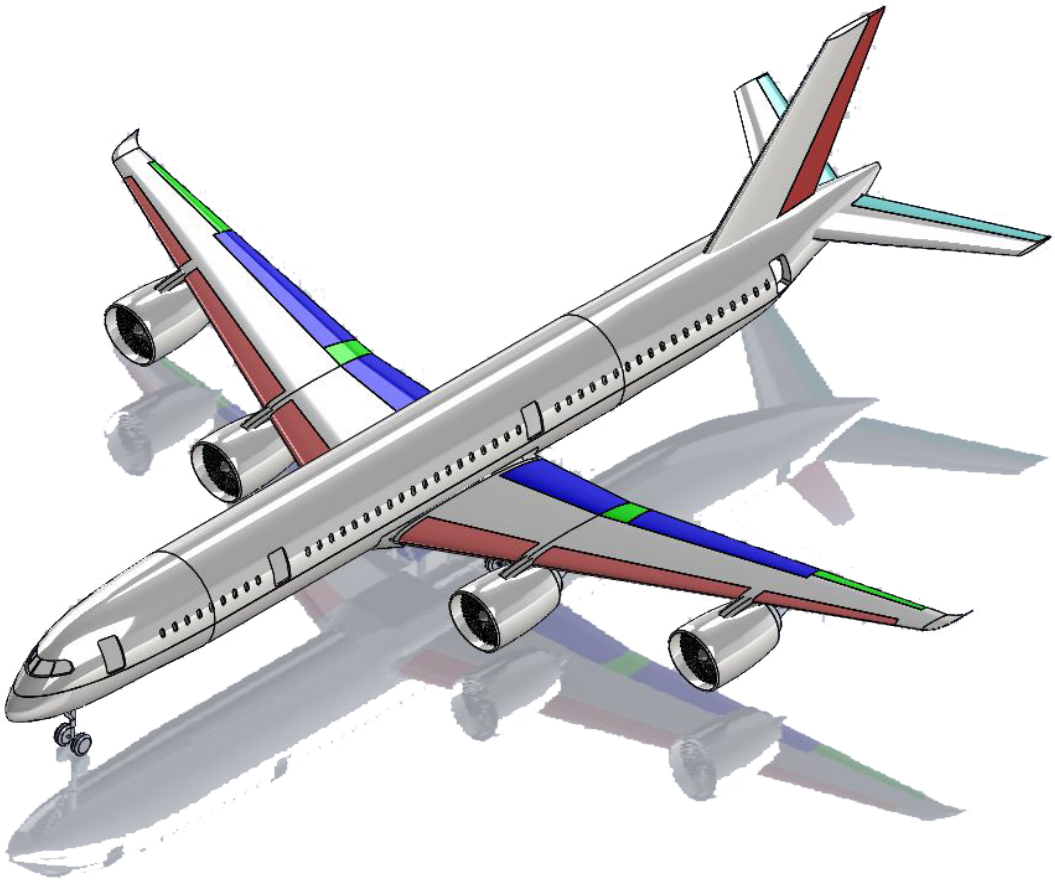

David Birkenheier, Nicholas Chan, Rehan Nawaz,
Jin Woo Park, Ryan Patterson, Conor Vander Hoff

December 13, 2015

Contents

List of Figures

List of Tables

1 Summary

1.1 Executive Summary

Singapore Airlines is interested in a long range aircraft to take 125 business class passengers on a nonstop flight from Newark to Singapore. The aircraft must be able to fly the 8285 nautical miles between the two airports, and also fly an additional 200 nautical miles from its reserves. The plane needs to enter the market in 2025, and must comply with part 25 of the FAR regulations while remaining profitable by minimizing cash operating cost (COC). Airbenders Ltd. has been contracted to design the aircraft that will satisfy this mission. The purpose of this report is to present the conceptual design of the aircraft that will satisfy this mission, and to outline the optimization of our preliminary design.

In the time since the preliminary design review, we have developed, validated, and implemented a multi-disciplinary design optimization software, allowing us to produce an airplane with the minimum cash operating cost while meeting all of the necessary constraints. This software utilizes improvements to our models including more accurate weight estimation formulas for the wing and fuselage, a more detailed analysis of viscous drag, the use of the Athena Vortex Lattice aerodynamics solver to model induced drag, and a more accurate segment-based fuel fraction calculator for the climb and cruise flight segments. The software also enforces all necessary constraints, resulting in the output of a design that requires minimal modifications in post-processing. The format of the software is such that we were able to use it in conjunction with a common gradient-based optimizer to find the aircraft with the minimum cash operating cost that meets all of the specifications and requirements of this mission. Utilizing this software, optimizations were performed on both two- and four-engine configurations, and it was found that a four-engine configuration allows for a lower cash operating cost. This insight led to a further reduction in the cash operating cost of the aircraft.

Additionally, following our critical design review presentation, we implemented several improvements to our model at the recommendation of the review board, including a more accurate equation for drag coefficient as a function of lift coefficient, inclusion of wave drag as a function of wing sweep angle, and a small change to our fuel storage in order to improve our center of gravity excursion. Using these additions, we re-optimized our airplane and found a new design point with a cash operating cost several thousand dollars lower than previously. This rapid re-optimization is a testament to the utility of our software, which outputs a nearly fully designed airplane.

The interior layout of the aircraft has been designed around the comfort of the passengers and crew while still maintaining efficiency and cost-effectiveness. This area includes the passenger seating and amenities, the cockpit, and the crew resting areas and galleys. The passenger seating is designed in a 2-2-2 configuration with an innovative offset seating arrangement to exceed business class specifications by providing full lie-flat seating for every passenger that is not only flat but also parallel to the floor of the cabin, while still providing for direct aisle access from window seats. The cockpit is designed to allow the pilot the full range of visibility specified by FAR requirements. Standardized containers were used to store the passenger luggage to ease the integration of this aircraft into the Singapore Airlines fleet, and fuel containers stored in the wings and the wing box of the aircraft can carry all of the fuel required for this long-range flight.

This design is capable of carrying out the desired mission with both maximum economic efficiency and exceptional passenger comfort. Finally, it provides for future growth by using an engine that is at the bottom of the thrust range for its line of engines. This allows for the easy integration of a higher thrust engine, which in turn would allow for the carriage of extra cargo or more passengers to further increase profitability.

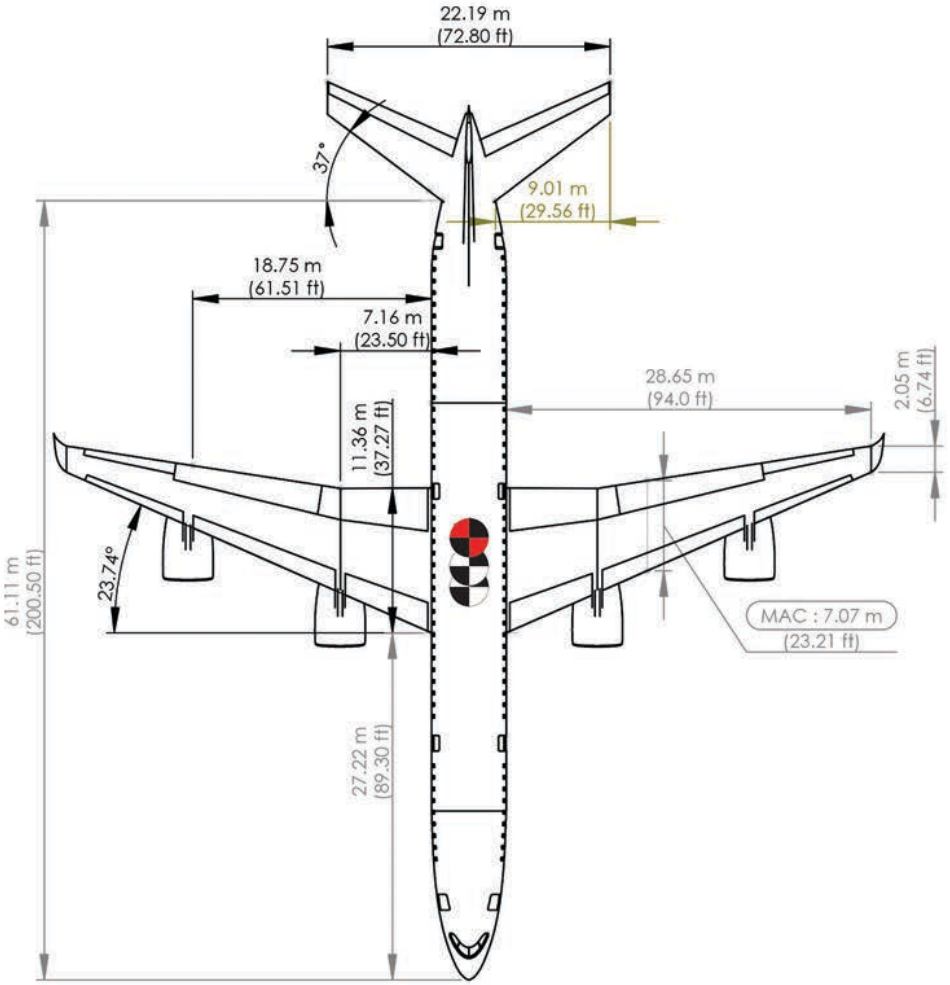
22.19 m
(72.80 ft)
37°
9.01 m
(29.56 ft)
18.75 m
(61.51 ft)
7.16 m
(23.50 ft)
28.65 m
(94.0 ft)
2.05 m
(6.74 ft)
11.36 m
(37.27 ft)
23.74°
61.11 m
(200.50 ft)
MAC : 7.07 m
(23.21 ft)
27.22 m
(89.30 ft)


Center of Gravity
Neutral Point

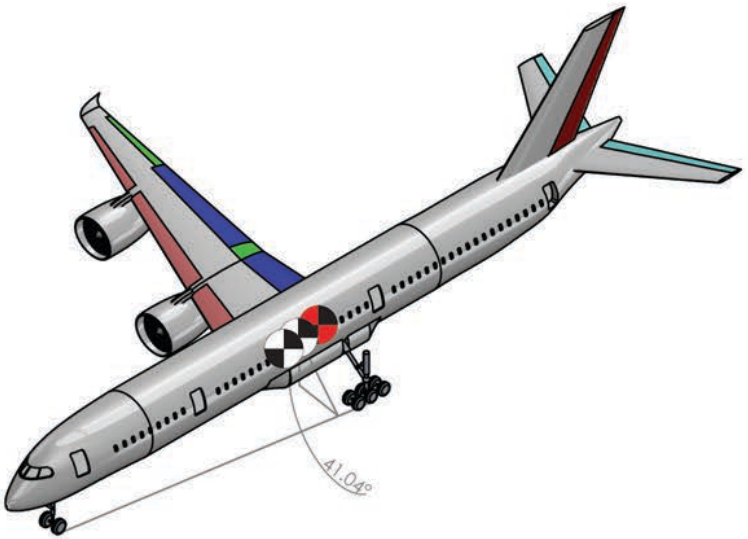
41.04°

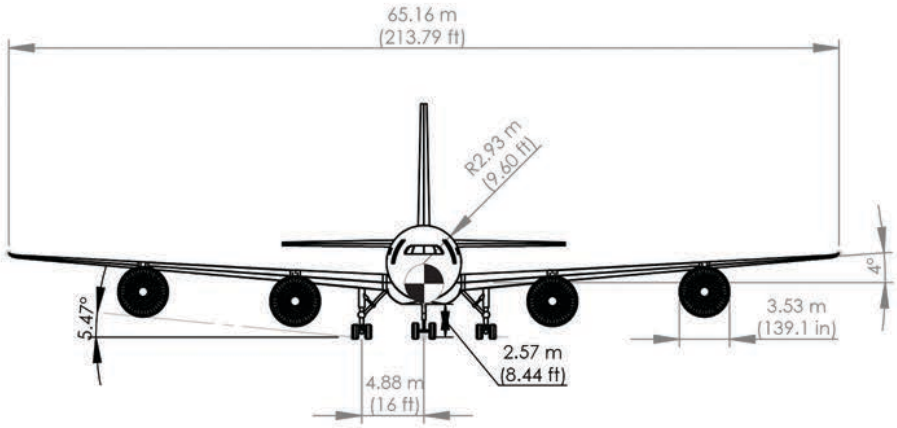
65.16 m
(213.79 ft)
R2.93 m
(9.60 ft)
4°
5.47°
3.53 m
(139.1 in)
2.57 m
(8.44 ft)
4.88 m
(16 ft)

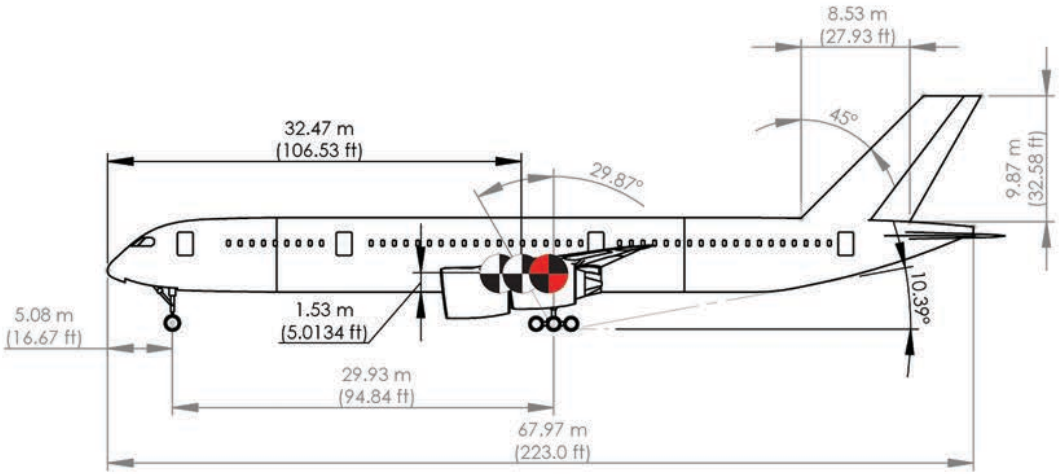
8.53 m
(27.93 ft)
45°
32.47 m
(106.53 ft)
29.87°
9.87 m
(32.58 ft)
10.39°
1.53 m
(5.0134 ft)
5.08 m
(16.67 ft)
29.93 m
(94.84 ft)
67.97 m
(223.0 ft)

1.2 Comparison Aircraft Parameters

To obtain a strong foundation of data from which to compare our plane's parameters, our team researched various airplanes that made similar flights, or had a similar range to our intended mission of making a nonstop flight between Singapore and Newark. The comparison included the B-787, the B-777, and the A-350. Here, we took data on many characteristics of these planes, the most important being their range, takeoff weight, empty weight and takeoff thrust.

Along with this, our team also looked into different engines, reviewing specific fuel consumption, engine weight and takeoff thrust, as the rate fuel is used up by the aircraft is a critical parameter in making the nonstop flight possible, as well as cost efficient. Here, the engines considered included the GEnx [1], GE90-115B [2], Trent 900 [3], and PW1100 [4].

Finally, we consolidated all of the various aircraft onto a single graph, utilizing a logarithmic regression of each plane's takeoff weight versus its empty weight to create a fitted equation that would be used to help create an accurate weight estimation to begin our design. For clarity, here are some of the closest aircraft in terms of parameters and overall design, in Table 1.

Table 1: Comparison of design with existing aircraft

Parameter	Design	B777-200LR	787-8	A350-900
Takeoff Weight,kgf (lbf)	256,407 (565,280)	347,500 (766,000)	228,500 (502,500)	268,750 (592,900)
Empty Weight,kgf (lbf)	118,528 (261,309)	145,150 (320,000)	118,000 (259,900)	115,711 (255,100)
Sweep Angle, deg	23.74	31.64	32.2	31.9
Fuselage Length, m (ft)	68 (223)	63.7 (209.1)	56.7 (186.1)	66.9 (219.5)
Fuel Capacity, L (Gal)	148,149 (39,137)	181,283 (47,890)	126,372 (33,384)	138,001 (36,456)
Engine and Thrust,kN (lbf)	GEnX-1B40, 118 (40,000)	GE90-115B, 512 (115,300)	Trent 1000, 320 (71000)	Trent XWB, 374 (84,000)
Span,m (ft)	57.3 (188)	64.8 (212.8)	60.1 (197.3)	64.8 (212.8)
Cruise Mach	0.83	0.84	0.85	0.89
Range,km (nmi)	15,344 (8,285)	15,800 (8,555)	14,100 (7,635)	14,350 (7,990)
Passenger Cap.	126	400	242	315
COC, USD	423,013	511,570	373,470	416,170

Along with this, below in Table 2 are some of our design's primary characteristics of flight, such as its wing loading and thrust-weight ratio, along with its coefficients of lift at various points in flight.

2 Introduction

Airbenders Ltd. has been contacted by Singapore Airlines to design a concept that resumes their nonstop flight between Newark and Singapore, shown below in Figure 1. Previously, such a flight was achieved with an Airbus A340-500 but was deemed not profitable enough for consistent flights. Due to this, Singapore Airlines is looking for a long-range aircraft that minimizes its cash operating cost (COC), while flying in a business-class configuration to maximize economic profitability. This

Table 2: Parameters of designed aircraft

Parameter	Design
Payload, kg (lb.)	17,010 (37,500)
Cruise C_L	0.49
Takeoff C_L	2.00
Landing C_L	2.50
Cruise L/D	16.7
T/W	0.28
W/S, Pa (lb./ft^2)	7121.66 (148.74)
Wing Reference Area, m^2 (ft^2)	353 (3800)
Aspect Ratio	9.3
Average Wing t/c	0.1
Static Margin (%MAC)	30.34 - 54.59
Max. Landing Distance, m (ft)	2,445 (8,023)
Max. Takeoff Distance, m (ft)	3,353 (11,000)

design will be ready for entry into service in the year 2025.

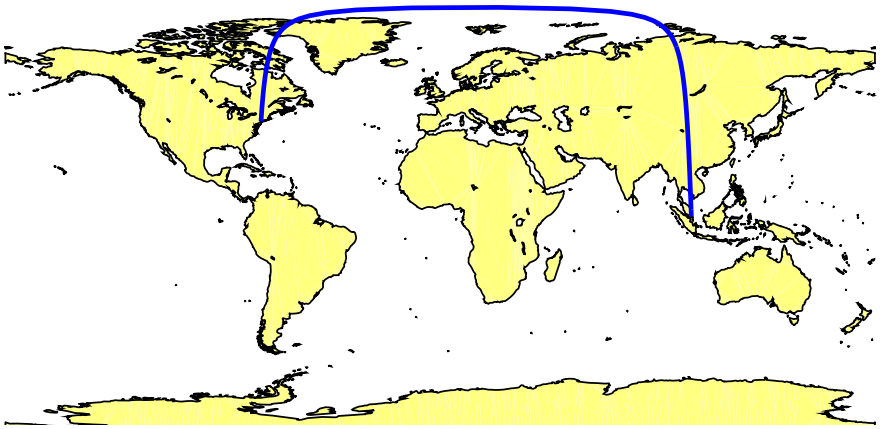

Figure 1: Great circle route from Newark to Singapore passes over North pole (8,285 nmi)

The design's mission profile shown below in Figure 2 is different from a typical mission profile, as it complies to the new NextGen initiative started by NASA and the FAA. In this updated profile, climb and cruise of the plane are optimized, with cruise sitting at around 35,000 ft., as well as both shorter taxi times and smaller fuel reserves (3% vs. 5%).

3 Interior Layout

The specification requires that our aircraft needs to provide a full lie-flat business cabin for 125 passengers. Current airliners implement various different business class configurations such as 1-2-1 or 2-2-2. The interior configuration chosen for this aircraft is 2-2-2, where every passenger has direct access to the aisle. There are two aisles with a width of 0.56 m (22 in) each. The three-view of the interior is shown in Figures 3, 4, and 5.

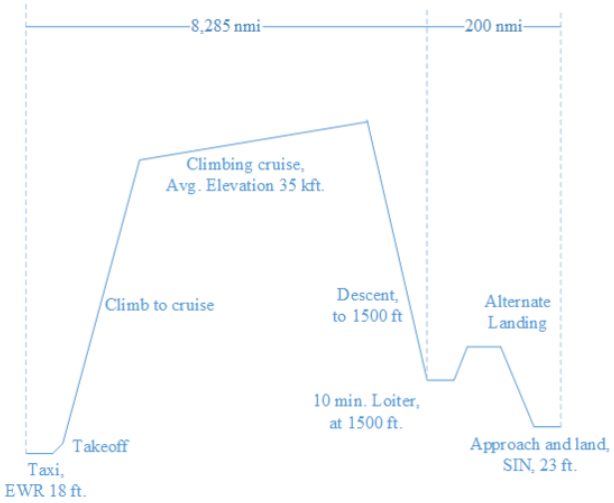

Figure 2: Next-Gen Mission Profile

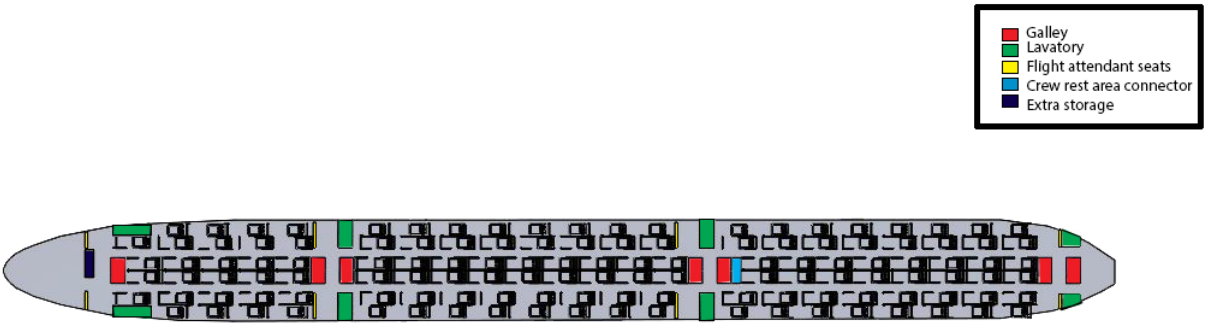

Figure 3: The top view of the cabin interior

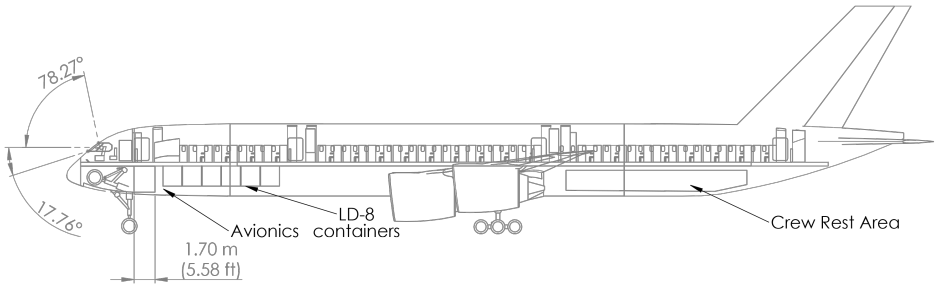

Figure 4: Aircraft side view with relevant interior dimensions

There are a few notable features of the interior design. First of all, the typical 2-2-2 configuration has a disadvantage with the window seat passenger lacking direct access to the aisle. However, our design has overcome this problem by offsetting the window side seats to give a 0.3048 m (1 ft) access path while providing 1.88 m (74 in) lie-flat seats for all passengers. Furthermore, the extra space generated due to the offsetting is used as a personal closet for each passenger (i.e., each passenger has a 15.2 cm (6 in) personal closet). This feature relieves the stress on the manufacturer to design

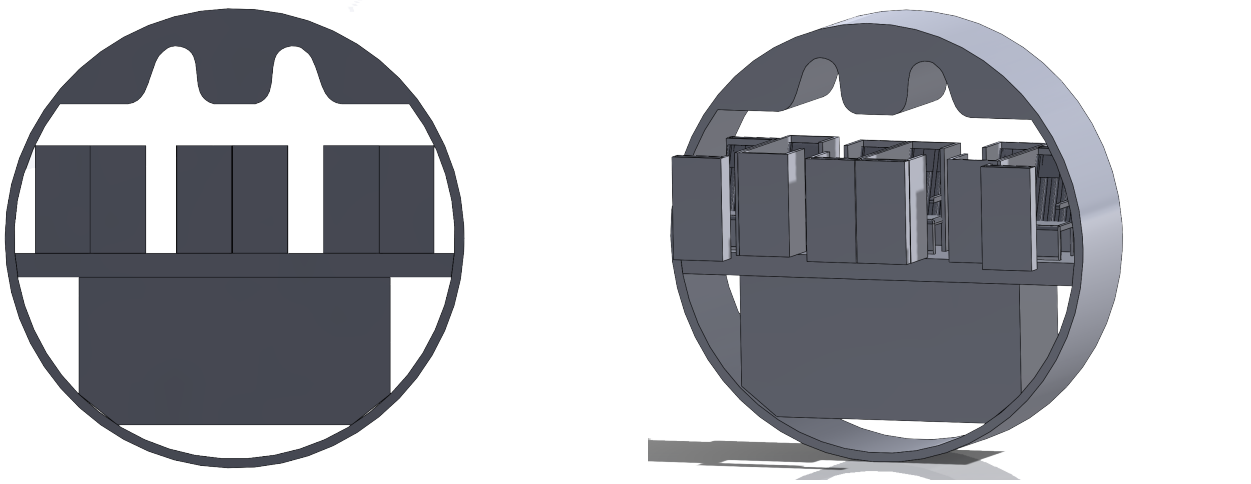

(a) Front view of the fuselage cross-section (b) The isometric view of the fuselage cross-section

Figure 5: The cross-sectional view of the fuselage

big closets in the cabin.

Secondly, there are seven galleys that can hold a total of 28 full size service trolleys. Considering that the estimated flight time from Singapore Changi airport to Newark airport is approximately 19 hours, the volume of food, beverages, utensils, and trash, etc for 125 business class passengers is going to be substantial. The volume of 6.3 m^3 (231.0 ft^3) provided by seven galleys is sufficient to place the aforementioned items.

Lastly, our aircraft design has a total of eight exits for expeditious evacuation of 125 passengers and fourteen flight crew and attendants in 90 seconds required to comply with FAR, Part 25. In addition, our design is capable of carrying eight smaller boats rather than four or six large boats in case of the ditching of the aircraft. This enhances redundancy in the case that a boat deflates or fails to inflate.

The crew rest area is located under and aft of the fuselage. The stairway connecting to the crew rest area is near the third galley from the empennage. This specific location of crew rest area is favorable, because the upper part of the fuselage can be dedicated to the overhead luggage compartment.

The flight attendant jump seats are located near the exit doors just as in typical aircraft. The four seats near the front and last exit doors are single seats. The second and third exit doors have two-person jump seats. Hence there are total of twelve flight attendant jump seats in this aircraft.

The cockpit length of our design is 4.21 m (165.7 in). Our design provides ample room for the cockpit, since a typical cockpit length is 3.81 m (150 in). The pilot vision angles for upper and lower bounds are 78.27° and 17.76° respectively. The detailed layout can be found in Figure 4. These angles satisfy the required pilot vision of 75° up and 17° down.

There is an additional extra storage space near the cockpit entrance for carry-on items bigger than the personal closet can accommodate. Avionics are located aft of the nose landing gear. Subsequently, six LD-8 luggage containers are placed in the front of the aircraft. The empty space between the luggage containers and the fuel tank could be dedicated to use for cargo shipping if the airline is looking to yield more profit.

4 Aerodynamics

The aerodynamic design of this airplane was done in large part by our optimizer. The parameters that define the wing geometry (reference area, span, taper ratio, and sweep angle) were set by the optimizer, in conjunction with other design variables, to yield the minimum cash operating cost. Thus the design decisions made with regard to aerodynamics were limited to the airfoil selection and the model to be used in the optimizer.

4.1 Airfoil Selection

Our airfoil selection is unchanged since the preliminary design review. We performed an extensive trade study, as described in Appendix B, and found that our numerical modeling tools were not trustworthy at the Mach number of interest, 0.83, and thus we turned to real data found in NASA technical reports from wind tunnel testing of NASA-designed airfoils. Using this data, we selected a theoretically designed shockless airfoil with a design sectional lift coefficient of 0.59. This exactly 0.1 above our final cruise C_L of 0.49. This is intentional, because the three-dimensional lift coefficient will be lower than the sectional lift coefficient seen by each airfoil due to 3-D effects, meaning that at our cruise C_L the airfoil will be operating close to its design C_l. The airfoil also has a maximum thickness-to-chord ratio of 0.10.

4.2 High-Lift Devices

The next step in wing design was sizing the high lift devices. Our design was based on an assumed takeoff C_L of 2.0 and landing C_L of 2.5, and these are important in determining the size of the aircraft because two of the limiting conditions are takeoff and balked landing climb, which are directly affected by their respective C_L's, so it is critical that our wing be able to achieve the desired C_L's for our airplane to be within the feasible design space. The shockless airfoil with no high-lift devices has a C_{lmax} of roughly 2.28, even before 3-D effects are taken into account; so at the very least, flaps were required. We performed a trade study considering flaps occupying 20, 30, and 40 percent of the airfoil chord deflected at 10°, 20°, and 30°. As can be seen in Figure 6, the 30 percent chord flap deflected at 30° had the best performance with a C_{lmax} of 2.55 at 14° angle of attack.

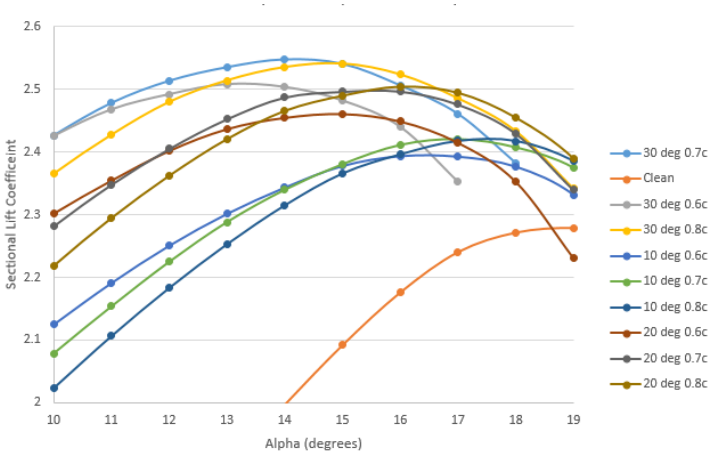

Figure 6: Performance of various flaps at 10°, 20°, and 30°

Even still, this is not enough to achieve a wing C_L of 2.5, so slats will also be required. In the

lecture slides there is a plot showing the effect of a 17 percent chord slotted slat on the performance of an airfoil in both its clean configuration and with two types of flaps deployed. The worst slat performance was with the double slotted flap deployed where it gave an increase in C_{lmax} of roughly 0.6. Assuming this performance for our flap, we should be able to achieve a C_{lmax} of 3.15, far enough above the desired 2.5 to make up for 3-D effects. We rounded the 17 percent of chord for the slat to 20 percent, to provide extra margin for what should be minimal extra weight. For types of flaps and slats, we chose single slotted to have the benefits of the reenergizing flow from below the wing being introduced into the boundary layer on the upper surface to delay separation without the extra weight required for multiple slots. This was especially true because we were already close to achieving our takeoff and landing C_L goals, so we did not need extreme performance improvements.

Knowing the spanwise locations of the ailerons from our stability and control analysis, we positioned the flaps everywhere not occupied by the ailerons, except for the 5 percent of the span outboard of the low speed aileron which is unused to avoid possible structural complexity in the narrowest part of the wing. This gave us flaps from 1 to 25 percent span and 30 to 70 percent span, with the flaperon from 25 to 30 percent span. We used as much span for slats as possible, from 1 to 95 percent span, again avoiding mechanical complexity in the narrowest part of the wing. Spanwise gaps were placed in the slats to allow for engine mounting.

4.3 Aerodynamic Modeling

Using these decisions as a basis, we then built our aerodynamic model to be used in the optimization. Since the initial estimation of the aerodynamics of the aircraft - which relied upon historical data for the cruise, takeoff and landing conditions - the aerodynamic model has been refined to take into account the geometry of the aircraft. Before, the basis of the aerodynamic model - the drag polar - had the form,

$$C_D = C_{D_0} + KC_L^2, \tag{1}$$

where C_D is the drag coefficient, C_{D_0} is the parasitic drag coefficient, C_L is the lift coefficient, and K is an aerodynamic coefficient for the induced drag KC_L^2. The updated version uses a more precise formula, first fitting a full quadratic to the induced drag, and then adding the C_{D_0}. This equation takes the form:

$$C_D = C_{D_0} + K_1C_L^2 + K_2C_L + K_3, \tag{2}$$

where C_{D_0} is the parasitic drag coefficient as before, and K_1, K_2, and K_3 are the coefficients of the induced drag quadratic. The use of this more precise method accounts for the fact that a cambered airfoil such as ours does not achieve zero lift at zero angle of attack, but actually at a somewhat negative angle of attack, and thus its drag polar is not symmetrical about the C_D axis. Using this formula, our results from AVL at any angle of attack match the values calculated using a regression from only three points to within the ten-thousandths place. By using a component build-up method for estimating C_{D_0} and utilizing the capabilities of AVL to evaluate many flight conditions and configurations for the aircraft geometry, a better model is obtained for working towards an optimized design. This model is described in detail below, and the resulting drag polar can be seen in Figure 7.

4.4 Parasitic drag coefficient by build-up method

In the component build-up method for the parasitic drag coefficient, the contributions of the individual components of the aircraft (e.g., fuselage, wings, tail, etc.) to C_{D_0} are evaluated and

summed together,

$$C_{D_0,comp} = \frac{1}{S_{ref}} \sum_{i=1}^{N_{comp}} C_{f,i} FF_i Q_i S_{wet,i} + C_{D,mis} + C_{D,leak}, \tag{3}$$

where S_{ref} is the wing reference area, $C_{f,i}$ is the skin-friction coefficient, FF_i is the form factor, Q_i is the interference factor, and $S_{wet,i}$ is the wetted area for component i. The contribution of each component to C_{D_0} is outlined in Table 3.

Table 3: Component drag contributions to C_{D_0}

Component	$C_{D_0,i}$
Fuselage	0.0053
Wing	0.0060
Horizontal tail	0.0014
Vertical tail	0.0011
Engines	0.0020
"Missing" drag due to fuselage upsweep	0.0037
Leak & protuberance drag	0.0006
Wave drag at $M = 0.83$	0.0010
Clean configuration	**0.0210**
Main landing gear bogeys	0.0171
Nose landing gear	0.0071
Flaps deflected by angle θ	$0.0480 \sin^2(\theta)$
Slats deflected by angle θ	$0.0205 \sin^2(\theta)$
Takeoff flaps (20°) and slats (10°)	0.0062
Landing flaps (30°) and slats (10°)	0.0126
Takeoff configuration	**0.0504**
Landing configuration	**0.0568**

4.5 AVL Modeling

One of the most important tasks undertaken since the preliminary design review was to incorporate more advanced aerodynamics into our analysis. In addition to the component buildup method used to calculate the new C_{D0}, we incorporated the use of a full plane model in AVL. This allowed us to capture the effects of trim drag along with the effects of the fuselage and nacelles. Using this new AVL geometry, and the C_{D0} from the component buildup method, we generated an asymmetrical drag polar by fitting a quadratic function to the induced drag, and then adding the C_{D0}. Our drag polar can be seen in Figure 7. This drag polar was created by running AVL at angles of attack up to 20° , and processing the results to find the angle at which either a section of the wing exceeded the sectional $C_{l,max}$ of our airfoil found from X-Foil or the rudder deflection exceeded 20°, signifying the loss of control authority. This angle was set as the maximum for the plot. Based on this method, we have a large margin between the C_L's of 2.0 and 2.5 set for takeoff and landing, respectively, and the true $C_{L,max}$'s of our wing, although this may also be due to errors in AVL at high angles of attack, or an error in our processing code as these $C_{L,max}$'s of roughly 3.1 and 3.6 seem very high. Irregardless, 2.0 and 2.5 are well within the capabilities of our wing.

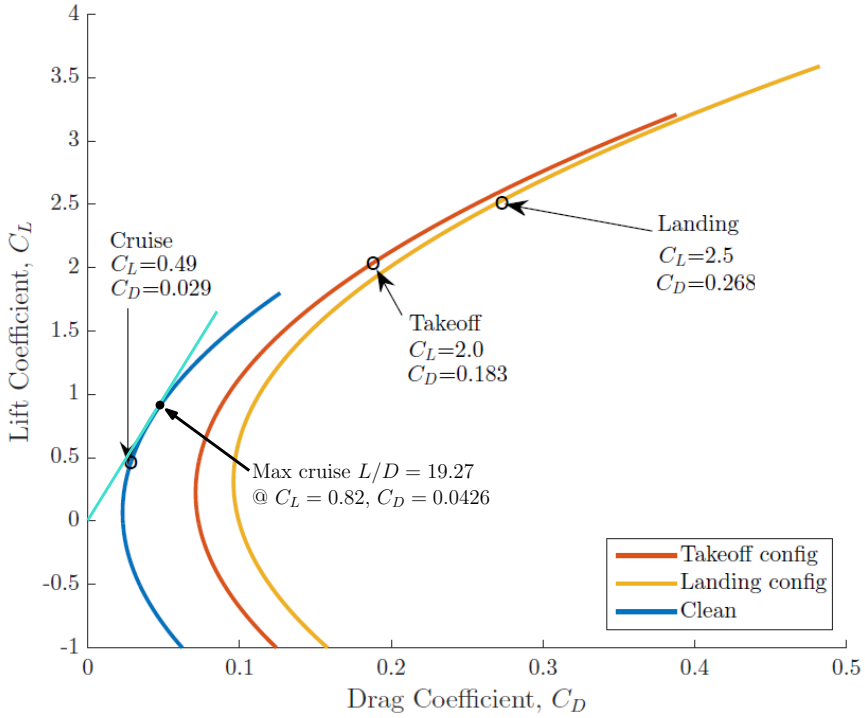

Figure 7: Drag polar generated using AVL and component buildup method

4.5.1 AVL Geometry

In order to attain accurate results from AVL, we needed to build an accurate model of our airplane. We used the 737 example from the AVL web page as a template. Once the interior layout was finalized, relatively early in the process, the fuselage dimensions were set. We used two perpendicular flat surfaces to represent the aerodynamic effects of the fuselage. One surface represented the top view of the fuselage, and the other the side view. The wing geometry remained the same as before the PDR in terms of the fractional locations of the flaps, slats, ailerons, and Yehudi break. Our AVL geometry file generator function already created a wing based on these percentages and the given reference area, span, taper ratio, and sweep. The wing also used our Garabedian shockless airfoil, which, being described in a NACA report that was a scanned version of a paper copy, required typing the airfoil geometry coordinates into a text file by hand. We added sections for the stabilizers using the same strategy, inputting reference area, taper ratio, aspect ratio, and sweep to calculate the necessary values to define the geometry. The stabilizers were placed according to the proper lengths calculated earlier in the program. Those surfaces used the NACA(SC)-0012 airfoil, which is supercritical to provide low drag at transonic conditions but also symmetric. All other sections did not have airfoils defined. We also included engine nacelles, using a surface shaped into a cylinder. The geometry file generator function took the number of engines as an input, and if there were two engines, it would only define two nacelles at the end of the Yehudi break at twenty-five percent span, but if the number of engines was four, it would define those two nacelles, and two more at two-thirds span. The control surfaces included were the inboard flap, slat, outboard flap, high-speed aileron, low-speed aileron, full horizontal tail, elevator, and rudder. The high-speed aileron acts as a flaperon in that the inboard flap is defined in that region as well so deflecting the inboard flap changes the datum of the high-speed aileron. All of these surfaces are included in a single component, which we found made a significant impact on modeling the flow correctly around

the intersection of the wing and the fuselage. The final geometry can be seen in Figures 8 and 9 and sample results are shown in Figure 10. The sample result is for the takeoff condition, showing the deflection of many of the surfaces, including both inboard and outboard flaps, slats, full horizontal tail, and elevator. There is a noticeable spike in the sectional lift coefficient where the wing meets the fuselage, but this was also observed when running the 737 example geometry file provided on the AVL web page, suggesting that it is correct. Critically, the creation of this geometry file was done automatically every time our code ran. This was a requirement for optimization, because the code needed to be able to generate its own AVL files in order to asses the aerodynamic performance of each design.

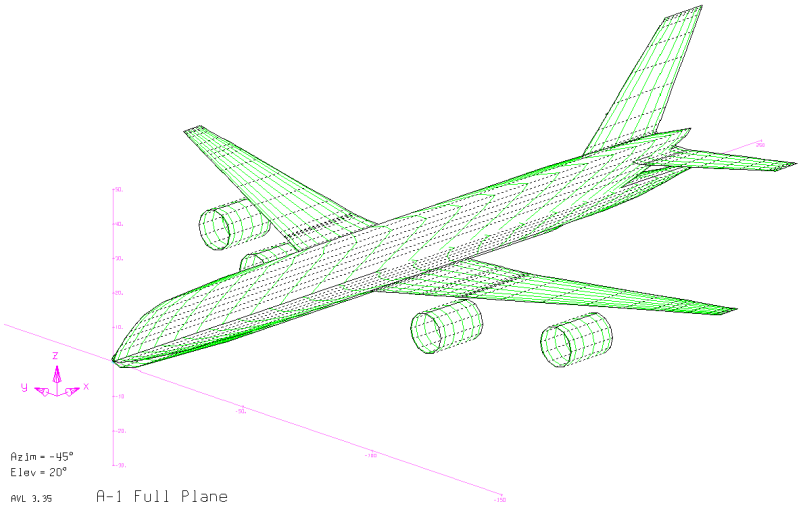

Figure 8: Isometric View of Final Geometry Shown in AVL

4.6 Final Wing Geometry

The optimized wing design found by our code has a surface area of 353.03 m^2 (3,800 ft^2), a span of 57.3 m (188 ft), a sweep angle of 23.7°, and a taper ratio of 0.2. This gives an aspect ratio of 9.3, which is in the range of those of current aircraft flying similar missions. This wing allows for a cruise C_L of 0.49, providing a cruise lift-to-drag ratio of 16.7, or $0.866\frac{L}{D}_{max}$. Our next-generation flight profile includes a climbing cruise segment, allowing us to maintain this optimal lift-to-drag ratio for the duration of our cruise segment.

4.7 Stall speeds

Using the data from the drag polar for cruise, takeoff and landing, the stall speeds can be calculated for these flight conditions according to,

$$V_{stall} = \sqrt{\frac{2W}{\rho C_{L,max} S_{ref}}}, \tag{4}$$

where W is the weight, ρ is the density of air, $C_{L,max}$ is the maximum lift coefficient achievable in the configuration, and S_{ref} is the planform area of the wing. In the takeoff configuration, the gross takeoff weight is used for W, the density of air at the elevation of Singapore at a temperature of

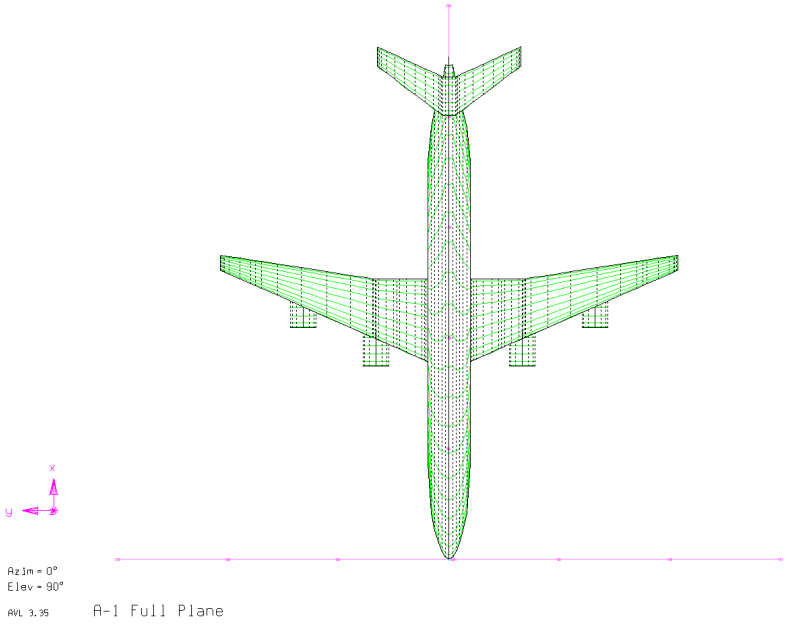

Figure 9: Top View of Final Geometry Shown in AVL

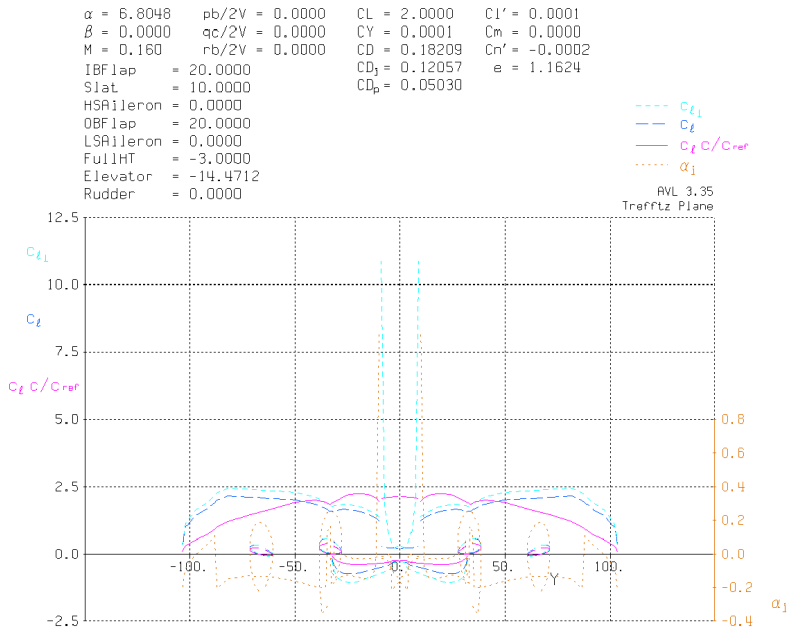

Figure 10: Sample output from AVL showing control surface deflections and aerodynamic performance at the takeoff condition

100°F is used, and $C_{L,max}$ is that found in AVL for the takeoff deflections of the high-lift devices. The landing configuration is similar to the takeoff configuration, except the weight used is the maximum landing weight and the greater deflection of high-lift devices at landing gives a larger $C_{L,max}$. For cruise, the weight considered is that at the end of the climb segment of the flight and

the altitude is the cruising altitude of 10,668 m (35,000 ft). The calculated stall speeds for these flight conditions are shown in Table 4.

Table 4: Stall speed calculation for flight conditions

Flight condition	Weight, kgf	Altitude, m	Density, kg/m^3	V_{stall}, m/s (kts)
Cruise	249,476	10,668	0.380	142.3 (276.5)
Takeoff	256,407	5	1.135	62.5 (121.5)
Landing	187,306	5	1.135	53.4 (103.8)

4.8 Maximum takeoff and landing distances

In addition to the stall speeds, the takeoff and landing distances required for the aircraft can be calculated. The takeoff distance is given by the balanced field length,

$$\text{BFL} = 37.5 \frac{W_{TO}/S_{ref}}{(\rho/\rho_{SL}) C_{L,TO} T_{TO}/W_{TO}}, \tag{5}$$

where T_{TO} is the takeoff thrust and $C_{L,TO}$ is the lift coefficient at takeoff - chosen to be 2.0. For the case of low air density due to a temperature of 100°F at either of the airports, the balanced field length is calculated to be 3,353 m (11,000 ft). Thus, this is the maximum distance that the aircraft will need to take off and exactly meets the constraint of the shorter of the longest runways available at Newark and Singapore airports.

The landing distance - with a 60 percent safety margin - is given as,

$$s_{FL} = \frac{1}{0.6} \left[5 \frac{W_{land}/S_{ref}}{(\rho/\rho_{SL}) C_{L,max,L}} + 300\text{m} \right], \tag{6}$$

where W_{land} is the maximum landing weight and $C_{L,max,L}$ is the lift coefficient achieved in the landing configuration. With our maximum landing weight given as 73.1% of the gross takeoff weight and a value of 2.5 chosen for $C_{L,max,L}$, the maximum landing distance needed for this aircraft is 2,445 m (8,023 ft). This gives a margin of 27% on the landing distance at an 11,000 ft runway.

4.9 One engine inoperative consideration

In order to ensure the airplane will always be controllable, we needed to ensure that the rudder can generate sufficient yawing force to counteract the thrust imbalance generated when one of the outboard engines fails. To do this, we first calculated the yawing moment produced by one engine out at full takeoff thrust, the worst-case scenario,

$$C_n = \frac{y_{eng} T_{0,Eng}}{\frac{1}{2} \rho V_{TO}^2 S_{ref} b}, \tag{7}$$

where $T_{0,Eng}$ is the maximum takeoff thrust of a single engine, and then set our rudder in AVL to generate this moment. The resulting plot can be seen below in Figure 11, showing that our rudder is capable of keeping the plane stable in the one engine out condition with a deflection less than 20 degrees, ensuring control authority.

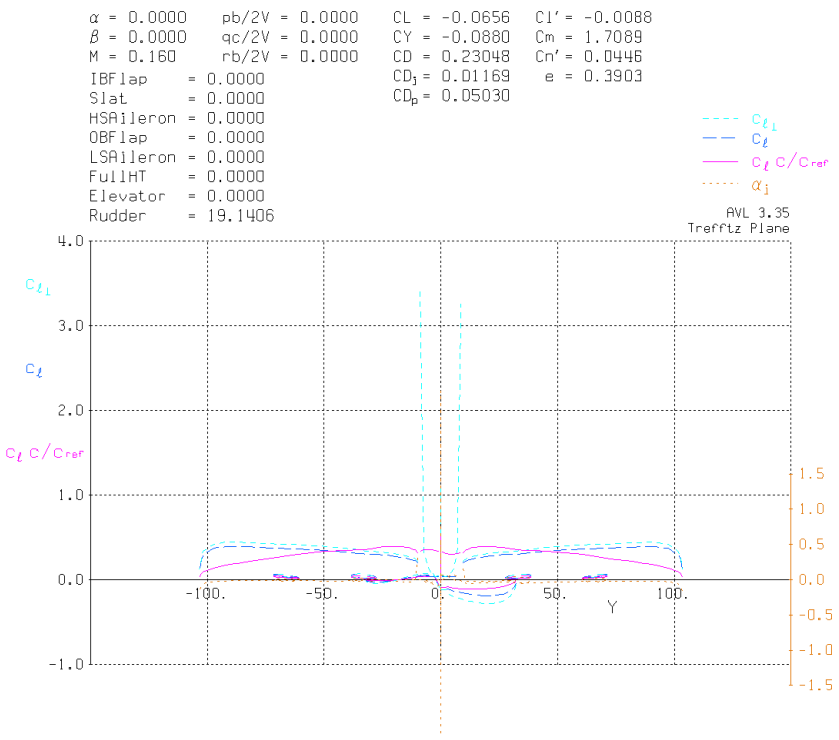

Figure 11: Airplane can be trimmed in one-engine-out condition

5 Weights and Center of Gravity

In order to obtain a more realistic estimate of the gross takeoff weight of the aircraft than what was initially calculated, a refined weight estimation scheme is implemented - whereby the weights and locations of different components are estimated individually. By summing the weights of the components (fuselage, wings, tail, etc.) we get an estimate of the takeoff weight. Additionally, by summing the moments of the components' weights about a datum - the nose, for example - we obtain an estimate of the location of the aircraft's center of gravity (CG). This information can further be used to estimate the necessary size of the landing gear and tires, as well as to analyze the stability of the aircraft. Table 5 shows the component weights for the aircraft, organized into weight groups.

5.1 Updated weight models

The weight models updated since the preliminary design review included those for the wing and fuselage. The wing weight model used is,

$$W_{wing} = 0.0051(W_{dg}N_z)^{0.557}S_w^{0.649}Æ(t/c)_{root}^{-0.4}(1+\lambda)^{0.1}(\cos\Lambda)^{-1}S_{csw}^{0.1} \tag{8}$$

where W_{wing} is the weight of the wing, W_{dg} is the design gross weight, which is the maximum takeoff weight, N_z is the maximum load factor, which is 2.5 for this plane, S_w is the wing reference area, $Æ$is the aspect ratio, t/c_{root} is the thickness-to-chord ratio at the root of the wing, λ is the taper ratio, Λ is the sweep angle, and S_{csw} is the control surface area. In implementing this function, there was ambiguity as to whether S_w was the wing reference area or the wing wetted area, which is roughly double the wing reference area. In order to check the accuracy of both, we performed

Table 5: Component weight distribution

Group	Component	Weight, kgf.	(lbf.)
Empty	Fuselage	23,429	(51,651)
	Wing	29,342	(64,687)
	Horizontal tail	1,930	(4,255)
	Vertical tail	1,768	(3,898)
	Engines	13,279	(29,275)
	Landing gear	5,786	(12,757)
	All else empty	43,589	(96,098)
Cargo	Luggage	6,994	(15,420)
Fuel	Wing tanks	99,154	(218,597)
	Fuselage tank	19,789	(43,628)
Crew	Pilots, Attendants	1,143	(2,520)
Payload	Passengers	10,206	(22,500)
MTOW	**All**	**256,407**	(**565,280**)

a validation of the wing model by finding the necessary parameters for several wings whose true weights were listed in Roskam [5], and inputting those values into the wing weight equation. The results are listed in Table 6. On average, using reference area gives a wing weight 25.3 percent below

Table 6: Wing Weight Validation

Aircraft	True Wing Weight (lbs)	S_{ref} Weight (lbs)	% Diff	S_{wet} Weight (lbs)	% Diff
DC-8	27,556	21,485	-22.0	33,691	22.3
DC-9-10	9,470	5,928	-37.4	9,297	-1.8
MD-80	15,560	10,642	-31.6	16,688	7.2
DC-10-30	58,859	49,038	-16.7	76,895	30.6
B737-200	10,613	7,325	-30.9	11,486	8.2
B747-100	86,402	75,079	-13.1	117,730	36.3

the true value, whereas using wetted area gives a wing weight 17.1 percent above the true value. In order to avoid moving forward to detailed design with an estimated wing weight drastically below what would be required structurally, we applied a factor of 1.25 to the weight obtained using reference area in (8) when calculating our wing weight.

The fuselage weight formula utilized for this analysis was the GD method found in Roskam [5, Vol. V],

$$W_{fuse} = 10.43(K_{inl})^{1.4}\left(\frac{q_D}{100}\right)^{0.283}\left(\frac{W_{to}}{1000}\right)^{0.95}\left(\frac{l_f}{h_f}\right)^{0.71}, \tag{9}$$

where W_{fuse} is the fuselage weight, K_{inl} is a factor to account for blended engine inlets that is equal to 1 in our case because our engines are wing-mounted, q_D is the design dive dynamic pressure, W_{to}

is the maximum takeoff weight, l_f is the length of the fuselage, and h_f is the maximum height of the fuselage. This gave us more representative fuselage weights than those given by simply applying a factor to the fuselage wetted area. We thus improved our estimations for the two most important structural components in terms of weight.

5.2 Refined fuel fraction

From our COC analysis leading up to the PDR, we found that the fuel cost takes up nearly 60% of the total COC. Due to this fact, there is a need for us to analyze fuel consumption as accurately as possible to obtain a realistic COC estimate. To do this, we reviewed our code related to fuel fraction computation and refined our method. Particularly, we modified the weight fraction computations in climb, cruise, and loiter.

Table 7: Summary of fuel fraction refinements

Mission Segment	PDR method	Refinements for CDR
Engine start,Warm up	Used Roskam's data	-
Taxi	Used Roskam's data	-
Takeoff	Used Roskam's data	-
Climb	Used Roskam's data	Multiple segment ; Best climb speed
Cruise	Breguet Range ; Roskam's L/D	Multiple segment ; Drag polar'sL/D
Loiter	Breguet Endurance ; Roskam's L/D	Drag polar's maximum L/D
Descent	Used Roskam's data	-
Reserves/Alternate	Breguet Range ; Roskam's L/D	-
Landing,Taxi,Shutdown	Used Roskam's data	-

5.2.1 Refinement of fuel fraction for climb

In the PDR, we merely obtained the value of weight fraction of 0.98 for climb from historical data given by Roskam. To refine this, we analyzed the fuel consumption in climb phase using a multi-segment approach.

First, the airspeed for best climb is calculated as,

$$V = \sqrt{\frac{W_i/S_{ref}}{3\rho C_{D_0}}\left(\frac{T}{W_i} + \sqrt{\left(\frac{T}{W_i}\right)^2 + 12C_{D_0}K}\right)}. \tag{10}$$

After the airspeed is calculated, we obtain the C_L based on the $L = W$ condition in steady flight during climb. With this C_L value together with our drag polar, we also obtain the C_D and eventually the drag for the sub-segment. Subsequently, the weight fraction of the sub-segment is calculated as,

$$\frac{W_{i+1}}{W_i} = \exp\left(-\frac{C_{climb}\Delta h_e}{V(1 - D/T)}\right), \quad where\ \Delta h_e = \Delta\left(h + \frac{V^2}{2g}\right). \tag{11}$$

It is also important that the distance of each climb sub-segment is credited to the range traveled:

$$x_{climb} = \frac{\Delta h_e}{P_S}V, \quad where\ P_S = \frac{V(T - D)}{W_i}. \tag{12}$$

5.2.2 Refinement of fuel fraction for cruise

In the PDR, we treated the cruise segment simply as one single segment with weight unchanged within the segment. This leaded to an overestimation of fuel consumption for cruise, especially for very long range missions similar to ours. Therefore, a multi-segment approach is utilized again for cruise for the refinement.

Calculating the maximum L/D from our drag polar as the location on the cruise line with the greatest positive slope, we used a cruise L/D of 0.866 of this value - or 16.7 - utilizing the climbing cruise of the "Next-Gen" flight profile. Subsequently, the weight fraction of the sub-segment is calculated using the rearranged Breguet Range Equation,

$$\frac{W_{i+1}}{W_i} = \exp\left(-\frac{R_i c_{cr}}{V(L/D)}\right), \tag{13}$$

where R_i is range of sub-segment i and c_{cr} is the cruise specific fuel consumption (SFC).

5.2.3 Refinement of fuel fraction for loiter

In PDR, we calculated the weight fraction for loiter using historical data given by Roskam. This resulted in a slightly higher fuel consumption. In the loiter refinement, we assume the airplane is flying at maximum L/D to minimize fuel burn. First, we use our drag polar to compute the maximum L/D value. After that, we compute the weight fraction of the loiter segment as,

$$\frac{W_{i+1}}{W_i} = \exp\left(-\frac{E c_{loi}}{(L/D)_{max}}\right), \tag{14}$$

where E is loiter time (endurance) and c_{loi} is the loiter SFC.

5.3 Fuel tanks

In order to store the nearly 120,000 kg of fuel (which equates to nearly 150,000 liters), the available volume within the wing box is utilized. By assuming that these in-wing tanks occupy 40% of the chord length (whereas the wing box occupies the 50% of the chord not taken up by high-lift devices), they account for 83% of the total fuel storage. This leaves the remaining 17% of the fuel (24,466 liters) to be stored in the fuselage - 715 liters of which can be stored in the wing-box carrythrough, with the remainder located in the remaining volume of the fuselage beneath the deck around the carrythrough and just forward of the wing box. The fuel tanks configuration is shown in Figure 12.

5.4 Center of gravity excursion

The center of gravity movement during loading and flight is shown in Figure 13. From this plot it can be seen that the total excursion from the most-forward to most-aft CG location is roughly 30 percent of the MAC, and the excursion during flight is roughly 25 percent MAC. This allows for a sufficiently small static margin to provide for control authority at all times.

6 Stability and Control

We decided to utilize the conventional tail configuration in our design. The major reason for this decision is that we would like to minimize the weight penalty caused by structural complexity. We

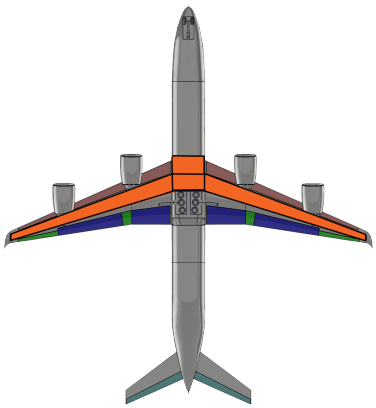

Figure 12: Fuel storage in wings, wing-box carrythrough and additional fuselage tank

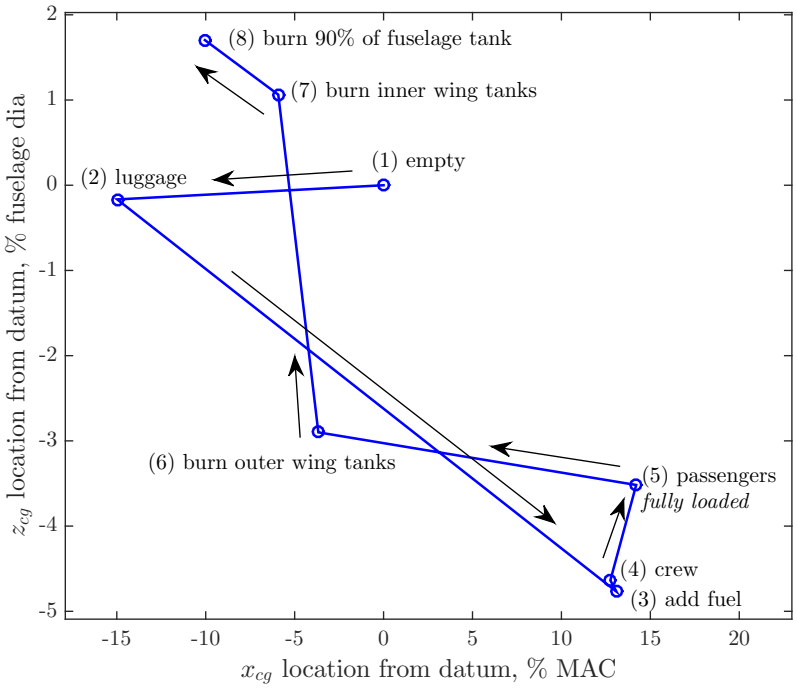

Figure 13: Center of gravity excursion through loading sequence

have also considered V-tail configuration since it could further reduce the weight and interference drag. However, we decided to retain the conventional design because the control via V-tail is highly non-linear. The control system development and the associated pilot training could be very costly and time consuming. The horizontal and vertical stabilizers are sized based on the volume coefficient method.

$$c_{VT} = \frac{L_{VT} S_{VT}}{b_W S_W} \tag{15}$$

$$c_{HT} = \frac{L_{HT} S_{HT}}{\bar{c}_W S_W} \tag{16}$$

Figure 14 below shows the parameters associated with the sizing of the horizontal and vertical stabilizers. The values for the volume coefficients for jet transport are chosen for our case. In

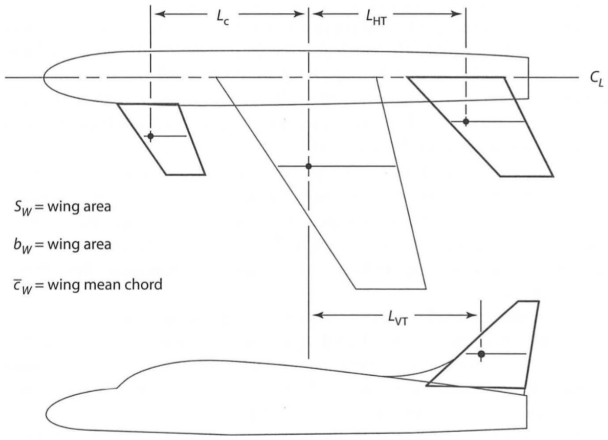

Figure 14: Areas and moment arms in the tail volume coefficient formulas [6]

addition, our horizontal stabilizer is an all-moving tail (i.e., adjustable angle of incidence), which can potentially induce a reduction on the horizontal tail volume coefficient by 10%-15%. Conservatively, we reduce the horizontal tail volume coefficient by 10%. As a result, the vertical and horizontal tail volume coefficients are chosen as 0.09 and 0.9 respectively.

The wing span, wing area, and the wing mean aerodynamic chord are obtained from our wing design section discussed previously. The calculation of the tail moment arm is described in detail below.

With the information above, the horizontal stabilizer area and the vertical stabilizer area are calculated as 71.87 m^2 (773.6 ft^2) and 65.85 m^2 (708.77 ft^2) respectively.

We assumed the preliminary planforms of the stabilizers to be trapezoidal surfaces. We determine the aspect ratios and taper ratios based on historical data [7]. In addition, the sweep angles are chosen using Roskams historical data [5]. The decisions are tabulated below:

Table 8: Selected aspect ratios, taper ratios and sweep angles for empennage

Parameters	Horizontal tail	Vertical tail
Aspect ratio, $\mathcal{AR}$	4.50	1.50
Taper ratio, λ	0.50	0.50
Leading edge sweep angle, Λ	37.0°	45.0°

With these values, all the dimensions for horizontal stabilizer and vertical stabilizer are calculated as shown in the empennage image in Figure 15.

6.1 Updated empennage sizing

In the initial sizing of the empennage - that is, the horizontal and vertical stabilizers - an approximation was made for the effective moment arms that each of the stabilizers have with respect to the aerodynamic center of the wing. By assuming that the aerodynamic centers of the tails were 55% of

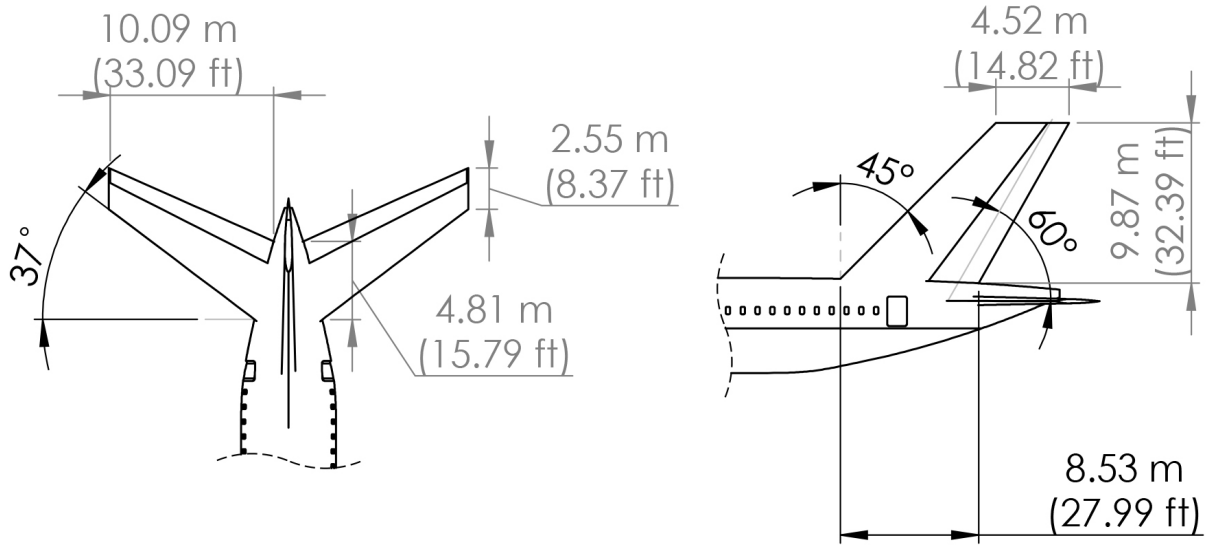

Figure 15: Empennage dimensions

the fuselage length behind the wing, the positions of the tails were at the mercy of the placement of the wing - giving the possibility of placing the tail too far back on the fuselage. Because we include an auxiliary power unit (APU) in the aft-most part of the tail cone at the back of the fuselage, the structural compatibility of the components of the empennage requires that both the horizontal and vertical stabilizers be forward of the APU.

Thus, in our updated sizing of the empennage we first fix the trailing edge of the horizontal stabilizer to be 1.54 m (5 ft) from the end of the fuselage and iterate the horizontal stabilizer planform area until the moment arm of its aerodynamic center to the wing aerodynamic center is converged. Only the planform area needs to be iterated in order to determine the correct moment arm between the aerodynamic centers of the lifting surfaces because the aspect ratio $\mathcal{AR}$, taper ratio λ, and sweep angle Λ are prescribed for the horizontal stabilizer as 4.5, 0.5, and 37° respectively. From these three parameters and the planform area, all other quantities pertaining to the geometry of the horizontal stabilizer can be determined - most importantly, the location of the aerodynamic center.

The iteration process begins with an initial guess for the moment arm between the aerodynamic centers L_{ht}^0 as the distance from the aerodynamic center of the wing to the beginning of the APU. From this moment arm, the planform area S_{ht} of the horizontal stabilizer is calculated to satisfy a volume coefficient C_{ht} of 0.9 (a value suggested by Raymer [8] for all-moving horizontal tails),

$$S_{ht} = \frac{C_{ht}\bar{c}_{wing}S_{wing}}{L_{ht}}, \tag{17}$$

where $\bar{c}_{wing}$ is the mean aerodynamic chord of the wing and S_{wing} is the planform area of the wing. From this value for S_{ht}, the root chord of the horizontal tail and thus the location of the leading edge of the horizontal tail are calculated. With this and $\mathcal{AR}$, λ, and Λ of the horizontal tail, the location of the aerodynamic center is calculated, allowing for an updated value of moment arm L_{ht}^n. If the residual between the calculated moment arm and the previous value $|L_{ht}^n - L_{ht}^{n-1}|$ is greater than the convergence tolerance, then the new moment arm is used as the starting point for another iteration of the planform area.

A similar process is used to calculate the size of the vertical stabilizer, also fixing the trailing edge to the beginning of the APU and using a volume coefficient C_{vt} of 0.09 (suggested by Raymer [8]), giving the planform area within an iteration as,

$$S_{vt} = \frac{C_{vt} b_{wing} S_{wing}}{L_{vt}}, \tag{18}$$

where b_{wing} is the span of the wing. The size of the vertical tail is converged upon in the same manner as for the horizontal tail; however, the blanketed area of the rudder by the horizontal tail in stall conditions needs to be less than two thirds of the total rudder area. The region blanketed by the horizontal tail stall is defined as the area behind the line that is 60° above the chord line of the horizontal tail from its leading edge, as depicted in Figure 15. As a preliminary measure to combat this effect within our design code, we translate the vertical tail forward according to an approximation of the offset needed to have the blanketed area be 2/3 of the total rudder area,

$$x_{vtTE} - x_{htTE} = \frac{\frac{2}{3} b_{vt}(1+\beta) + 0.35 c_{vt,root}}{(2+\beta)\tan 60°}, \tag{19}$$

where,

$$\beta = 0.35(\lambda_{vt} - 1)\frac{c_{vt,root}}{b_{vt}}, \tag{20}$$

with b_{vt} as the vertical tail span, $c_{vt,root}$ as the root chord of the vertical tail, and λ_{vt} as the taper ratio of the vertical tail. In order to ensure that this condition is satisfied, the fraction of the rudder area which is un-blanketed by the horizontal tail is checked in our CAD model. If the sizing and placement are such that this fraction of the rudder area is less than one third after the convergence upon a design point, we translate the vertical tail the residual distance forward.

6.2 Static margin determination

The static margin is a metric that allows for a preliminary quantification of the static stability of the aircraft, measuring the fraction of the mean aerodynamic chord length that the center of gravity is separated from the neutral point on the aircraft. The static margin is thus expressed as,

$$SM = \frac{x_{cg} - x_{np}}{\bar{c}}, \tag{21}$$

where x_{cg} and x_{np} are the locations of the center of gravity and the neutral point, respectively, and $\bar{c}$ is the mean aerodynamic chord. Because the determination of the neutral point requires the use of AVL, we use a simplified estimate for the static margin,

$$SM \approx \frac{C_{L_{\alpha ht}} S_{ht} l_{ht}}{C_{L_{\alpha w}} S_w \bar{c}} - \frac{x_w}{\bar{c}}, \tag{22}$$

from Martins [6] in our design code, not taking into account the effect that the fuselage has on the moments due to the lift distributions of the wing and horizontal stabilizer. This equation is used in lieu of AVL for expedience of calculation within our design code - allowing for the implementation of constraints on the static margin without having to run AVL more times when performing design optimization. With the convergence of the optimization on an aircraft which minimizes the objective function, we run the converged solution trough AVL to exactly calculate the location of the neutral point, and thus the exact value of the static margin by (21).

With the neutral point located 34.6 m (113.6 ft) from the nose of the aircraft, a mean aerodynamic chord length of 7.07 m (23.21 ft), and a movement of the CG from 32.5 m (106.5 ft) to 30.8 m (100.9 ft) through the flight - as calculated in Section 5 - the static margin for the aircraft is 30.34% MAC at takeoff and increases to 54.59% MAC during flight to a minimum-weight landing.

6.3 Control Surfaces

6.3.1 Ailerons

Our decisions on aileron sizing were made based on historical data. According to a graph from Raymer [8], aileron effectiveness depends on both spanwise size and chordwise size. Reading off the graph, if the ailerons occupy 30 percent of the chord, then they require roughly 30 percent of the span. We divided this span between the low speed aileron near the wingtip, and the high speed aileron just outboard of the Yehudi break, which ends at 25 percent of the span. The low speed aileron was given 25 percent of the span and the high speed aileron 5 percent of the span, because the high speed aileron operates at high-speed conditions when fast rolls are usually not necessary and a small deflection will cause a large change in lift because of the high velocity. The high speed aileron is a flaperon, meaning that when the flaps are deployed, the high-speed aileron deflects to the same degree as the flaps and then can further deflect about that new zero as an aileron.

6.3.2 Rudder

Our decisions on rudder sizing were made based on the rudder sizing of current transport aircraft. The span of the rudder is 100 percent of the vertical stabilizer span. It is sized as long as possible for two reasons. First, the long span would provide best maneuverability on yawing. Second, longer rudder span would increase the performance on spin recovery because more rudder portion would be unblanketed. The rudder chord at the inboard location is 35 percent vertical stabilizer chord while the rudder chord at outboard location is 30 percent vertical stabilizer chord. There are two reasons for this decision. First, by reducing the tip load relative to the root load, the adverse roll effect would be reduced. Second, since the tip load is reduced, the weight penalty from airframe structure will also be slightly reduced. We used AVL to ensure that our rudder had sufficient control authority to handle the most extreme yawing situation, an outboard engine failure during takeoff, as shown in Section 4.9.

6.3.3 Elevators

Our decisions on elevator sizing were very similar to those of the rudder sizing. The span of the elevator is 100 percent of the horizontal stabilizer span. This would give the best maneuverability in pitch. The elevator chord at the inboard location is 25 percent of the horizontal stabilizer chord while the elevator chord at the outboard location is 20 percent of the horizontal stabilizer chord. As stated before, the reduced tip load will lead to a smaller weight penalty from airframe structure.

7 Propulsion System

A key element of our design is our propulsion system. The engines are critical to the overall design because they determine the fuel efficiency, make up a major part of the weight of the aircraft, and set the upper bound on possible thrust. Several factors led us to explore the possibility of using more than two engines. First, one of the most restrictive constraints is the balked landing climb thrust loading constraint, which is dependent on the one-engine-inoperative thrust level. For a four engine plane, this level is three quarters of the nominal takeoff thrust, whereas for a two engine plane it is only one half of the nominal takeoff thrust. Thus, a four engine plane has a less strict balked landing climb constraint, which allows for lower takeoff thrust and thus lower takeoff weight, while also widening the feasible design space to allow for better optimization. The second major factor is the specific fuel consumption of the engines. The GE90 engines required for a two-engine plane

of this size have a relatively high thrust-specific fuel consumption, (TSFC), at 0.54 lbm/(lbf*hr). However, if we could reduce the takeoff thrust sufficiently by using four engines, we could use the GEnx engines, which have a lower TSFC at 0.51 lbm/(lbf*hr). This alone would greatly reduce our fuel weight and thus our cash operating cost. Finally, after increasing our fuselage size to accommodate beds that lie horizontal to the floor, and aisle access for every passenger, our weight increased significantly, requiring more thrust to meet the thrust loading requirements and putting us close to the upper limit of thrust attainable with two engines. This meant that we needed to include a four-engine option in our optimization in order to make sure we ended up with a feasible plane.

For these three reasons, we optimized two different designs, one with four engines and one with two engines. We then compared the results and selected the one with the lower cash operating cost. In order to allow for this double optimization, our code was written to allow for the use of two or four engines. Based on the number of engines, the code adapts the way it calculates the center of gravity, engine weight, thrust loading constraints, and AVL geometry file. The results of the two optimizations are shown in Table 9. They are very similar as the optimizer did not change either much from the same starting point. More details on the optimization process can be found in section 12.

Table 9: Comparison of optimizations performed on 2-engine and 4-engine configurations

Parameter	2-Engine Optimized Design	4-Engine Optimized Design
Reference Area, m^2 (ft^2)	353.29 (3,802.77)	353.1 (3,800.5)
Wingspan, m (ft)	57.30 (188.0)	57.299 (187.99)
Wing Leading Edge Position, m (ft)	27.26 (89.43)	27.22 (89.29)
Wing Loading, kg/m^2 (lb/ft^2)	771.4 (158.0)	726.0 (148.7)
Takeoff Weight, kg (lb)	272,477 (600,710)	256,407 (565,280)
Takeoff Thrust, kN (lbf), kg (lb)	789.16 (177,410)	699.22 (157,190)
Cash Operating Cost, USD	447,660	423,013

The four-engine plane has a significantly lower cash operating cost, and thus we chose to use a four-engine design. Interestingly, although one of the major factors in deciding to try a four-engine design was to lower the balked landing climb thrust loading constraint, both optimized designs were limited by the takeoff constraint. This may mean that an optimum design was found which is shifted to the left on the T vs. S plot to be on the takeoff thrust loading constraint rather than balked landing climb. However, because of the SFC advantage, the four engine design still proved to be superior. The thrust loading of the 2-engine design is 0.295, whereas that of the 4-engine design is 0.278, a difference of 0.017. This is a source of weight and fuel savings, but it is primarily due to the lower wing loading of the 4-engine design, rather than any manipulation of the constraint curves. Prior to finalizing this choice, we ensured that the aircraft could still be trimmed in a one-engine out condition where the outboard engine is without power, as described in Section 4.9.

Having chosen the four-engine configuration, we needed to select an engine. The thrust requirement for our final design ended up at 174.8 kN (39,300 lbf) per engine. This is lower than the 255.3 kN (57,394 lbs) given by the GEnx-1B54. However, the excellent thrust specific fuel consumption of the GEnx still made it the best available option. We will thus work with GE to develop a derivative of the GEnx, the GEnx-1B40, that develops 177.93 kN (40,000 lbs) of thrust for the same SFC, and consequently weighs less than the current GEnx options. Table 10 shows various engines close to our needed thrust, including our selected engine.

Table 10: Comparison of Engine Options (* denotes an estimated value)

Engine	Takeoff Thrust, kN (lbs)	SFC, g/(kN-s) (lb/(lb-hr))	Dry Weight, kg (lbs)
GE90 - 115B	513.9 (115,540)	15.3163 (0.540)	8,283 (18,260)
Trent 900	374.1 (84,096)	15.521 (0.5472)	6,246 (13,770)
PW1100G-JM	160.0 (35,000)	13.61 (0.48*)	2,857 (6,300)
GEnx-1B54	255.3 (57,394)	14.46 (0.51)	6,147 (13,552)
GEnx-1B40	177.93 (40,000)	14.46 (0.51)	3,319 (7,319)

Using an engine at the lower end of its line's thrust range allows for future growth. Had we chosen an engine with less thrust than we need and worked with the manufacturer to build a higher-thrust version, that would have put us at the upper limit of that engine's thrust range, eliminating the possibility of any larger versions of the plane in the future. Currently our payload weight is low because we have few passengers relative to the size of our plane. However, it may increase profit to fly cargo in addition to the passengers. We would still be able to meet all FAR thrust loading constraints easily using variants of the GEnx engines. It may also prove more profitable to add an economy class section to the plane. This would also increase the payload weight, which would be possible with our thrust margin.

8 Landing Gear

With the majority of the aircraft accounted for in the calculation of the weight and center of gravity, what remains is to size the landing gear to satisfy constraints on the height of the gear. These include the lateral (spanwise) and longitudinal (lengthwise) tip-over angles and the rotation clearance angle. The goal is to determine the minimal height of the landing gear such that all three of these constraints are satisfied.

8.1 Lateral tip-over

The constraint on the lateral tip-over angle is that the line connecting the bottom of the deflated tire on the main gear and the bottom of the wing-mounted engine be greater than 5° from the horizontal, as depicted in Figure 16.

The main landing gear is placed on the wing such that when retracted, only the tires are contained within the fuselage, with the remainder of the gear contained along the wing. This gives a relationship between the height of the landing gear h_{lg}, the tire diameter for the main gear d_{tire}, and the placement of the landing gear on the wing from the wing root y_{lg}:

$$y_{lg} = h_{lg} - d_{tire}. \tag{23}$$

With this, the minimum landing gear height needed to satisfy the 5° lateral tip-over angle is,

$$h_{lg,lat} = \frac{(y_{eng} + d_{tire})(\tan 5° - \tan \phi) + d_{eng}}{1 + \tan 5° - \tan \phi}, \tag{24}$$

where y_{eng} is the distance from the wing root that the engine is placed, ϕ is the dihedral angle, and d_{eng} is the diameter of the engine.

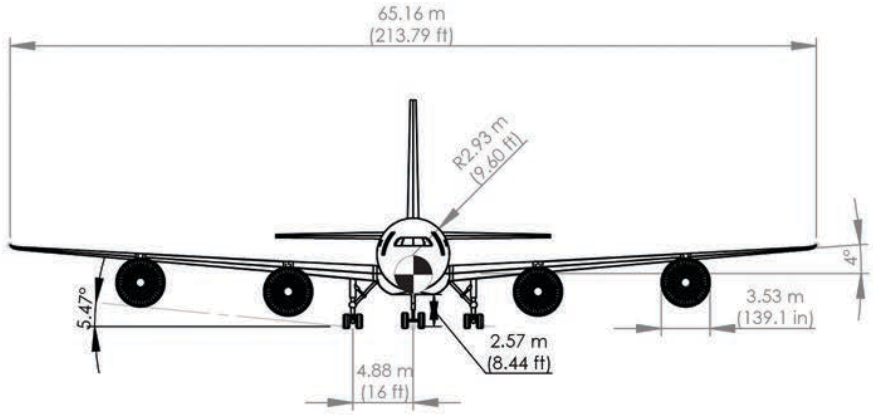

Figure 16: Front view of aircraft, showing lateral tip-over angle of 5.47°

8.2 Rotation clearance

The constraint on the rotational clearance angle is that the line connecting the bottom of the deflated tire on the main gear and the aft-most location on the underside of the fuselage before the tail cone be greater than the rotation angle encountered at takeoff. We determined through a run of AVL that the angle of attack necessary to achieve our takeoff C_L of 2.0 - and thus the rotation angle that will be induced at takeoff - is 6.8°, as shown in the AVL output in Figure 10. Going into the design optimization, we did not know what the aircraft's takeoff rotation angle would be; so, we used a conservative 11° constraint on the rotational clearance - an angle that can be seen in Figure 17.

The minimum landing gear height needed to satisfy the 11° rotation angle is,

$$h_{lg,rot} = \frac{\tan 11^\circ \ (l_{fuse} - l_{taper} - x_{lg}) - d_{tire} \sin\phi}{1 - \sin\phi}, \tag{25}$$

where l_{fuse} is the total fuselage length, l_{taper} is the length of the tail cone, and x_{lg} is the distance of the landing gear from the nose of the aircraft.

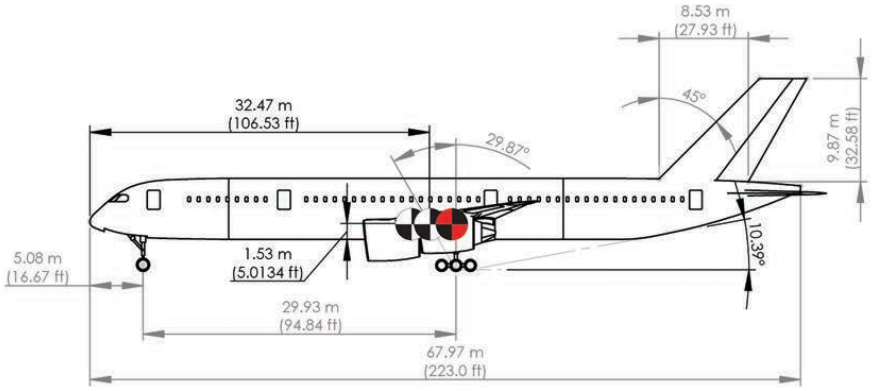

Figure 17: Side view of aircraft, showing longitudinal tip-over angle of 29.43° and rotation clearance angle of 10.39°

8.3 Longitudinal tip-over

The constraint on the longitudinal tip-over angle is that the line connecting the aft-most location of the center of gravity and the deflated center tire of the main gear be greater than 15° from the vertical, as depicted in Figure 17.

In contrast to the other two constraints on the landing gear, this constraint provides a maximum landing gear height which satisfies the 15° requirement,

$$h_{lg,long} = \frac{1}{1-\tan\phi}\left[\frac{x_{lg}-x_{cg,aft}}{\tan 15^\circ} + (r_{fuse}-d_{tire})\tan\phi - z_{cg,aft}\right], \tag{26}$$

where $x_{cg,aft}$ is the aft-most x-location of the center of gravity from the nose of the aircraft, r_{fuse} is the radius of the fuselage, and $z_{cg,aft}$ is the aft-most z-location of the center of gravity from the bottom of the fuselage.

In addition to these three tip-over angle constraints, there is also a constraint on the tip-over line which connects the deflated-tire nose and main gears. The perpendicular to this line which passes through the center of gravity must be less than 55° above the horizontal in order to maintain a stable configuration while the aircraft is on the ground. Because before our optimization of the aircraft design we noticed that this angle was not in the vicinity of the upper bound, we did not define a constraint on the necessary landing gear height to meet this tip-over requirement. In our finalized design, the assumption that this tip-over angle would not drive our design was proven to be valid as this angle was shown to be 41.04°, well under the requirement.

8.4 Synthesis of constraints

Because the constraints on the lateral tip-over and rotational clearance angles give the minimum landing gear heights needed to satisfy them, the greater of $h_{lg,lat}$ and $h_{lg,rot}$ will satisfy both of these constraints. With the maximum landing gear height constrained by the longitudinal tip-over angle, the bounds on the landing gear height are,

$$\max\{h_{lg,lat}, h_{lg,rot}\} \leq h_{lg} \leq h_{lg,long}. \tag{27}$$

In order to avoid the potential issue of obtaining $h_{lg,long}$ less than either $h_{lg,lat}$ or $h_{lg,rot}$, the landing gear height is chosen to be $\max\{h_{lg,lat}, h_{lg,rot}\}$ within the design code and the longitudinal tip-over angle is constrained externally (i.e., as part of the nonlinear constraints for `fmincon` iterations). Rearranging (26) gives the longitudinal tip-over angle in terms of the design variables,

$$\varphi_{long} = \tan^{-1}\left(\frac{x_{lg}-x_{cg,aft}}{z_{cg,aft}+(1-\tan\phi)h_{lg}-(r_{fuse}-d_{tire})\tan\phi}\right). \tag{28}$$

By specifying that this angle be greater than 15°, `fmincon` will be constrained to find solutions for the design of the aircraft which satisfy (27). With the x-location of the landing gear decidedly fixed with respect to the leading edge of the wing at 68% of the chord where the main gear is attached to the wing,

$$x_{lg} = x_{wingLE} + 0.68(c_{root} + y_{lg}\tan\Lambda), \tag{29}$$

the feasibility of the design by its satisfaction of the tip-over constraints is determined by the placement of the wing leading edge x_{wingLE} and the root chord of the wing c_{root}.

8.5 Coupling with CG location

Because the location of the aircraft's center of gravity is dependent on the size of the landing gear and because the size of the landing gear is dependent on the location of the center of gravity, a simple iteration is used to converge upon the landing gear size that satisfies the above constraints.

There are two modules in this part of the software through which this task is carried out: the CG location calculation and the landing gear sizing calculation. By supplying the CG location code with an initial guess for the landing gear height h_{lg}^0, the CG is calculated for this input, thus supplying the landing gear sizing with a CG input x_{cg}^0. From the landing gear sizing code, an updated landing gear height h_{lg}^n which satisfies (27) is calculated. The residual between the initial guess and the updated value for landing gear height $|h_{lg}^n - h_{lg}^{n-1}|$ is then calculated. If the residual is greater than the convergence tolerance, the updated height h_{lg}^n is fed back into the CG calculation.

8.6 Gear configuration

The landing gear configuration was chosen based on historical data and a size estimate of the aircraft. The tricycle configuration was chosen for the aircraft based on its stability and practicality, given the proximity of the gear to major mounting points for other components. Because the weight is between 180,000 kg (∼400,000 lbs) and 270,000 kg (∼600,000 lbs), a six wheel bogey configuration for each mid gear strut was chosen. The configuration is shown in Figure 18.

Figure 18: Landing Gear Configuration

8.7 Tire sizing

Next, tire size was taken into consideration. A regression developed by Raymer [8] for the sizes of the tires necessary to support the loads on the landing gears by the aircraft was used,

$$LG = AW^B \tag{30}$$

where A and B are constants that are determined by the type of aircraft for which the tires are being sized, and W is the weight that is loaded on each tire. The constants A and B change depending on whether the tire width or diameter is the sized parameter represented by LG. In order to get the loading on the tires on the mid landing gear, the position of the center of gravity relative to the mid landing gear was calculated, and the force was determined using moment and force balance relationships.

The following values were obtained for the sizes of the landing gear, shown in Table 11.

Table 11: Landing Gear Sizes

Parameter	Height m (ft)	Diameter m (ft)	Width m (ft)
Mid Gear	4.01 (13.17)	1.292 (4.24)	0.485 (1.59)
Nose Gear	2.57 (8.44)	1.195 (3.92)	0.430 (1.41)

8.8 Final placement

In order to place the landing gear, a combination of historical data and force and moment diagrams were used. The nose gear was placed 5.08 m (200 in.) from the tip of the nose. This was done because the length of the cockpit is 4.21 m (165.7 in.), and the landing gear needs to be placed after the cockpit to allow for room for storage during flight.

The main landing gear was placed to satisfy tip-over constraints, as well as rotation during the takeoff flight condition. The location of the landing gear is summarized in Table 12, and the constraints and values for tip angles are shown in Table 13. The rotation clearance angle of 10.39° is less than the artificial constraint of 11° that we specified in the design code (Section 8.2) because after obtaining our design from the code, we manually moved the landing gear aft on the wing to satisfy structural compatibility with the support in the wing for the gear. The design given from the design code, however *did* meet this 11° constraint. Because of our conservative estimate in the definition of the constraint, the violation of this as a result of moving the gear is still within the absolute constraint of the 6.8° rotation angle at takeoff. Also, the optimizer output a value for the longitudinal tip-over angle close to the 15° constraint, but by moving the main gear back in this manner, our final design has a value of 29.87° - a margin of nearly 15°.

Table 12: Landing gear placement

Parameter	Distance (m)	Distance (ft)
Nose gear distance from nose	5.08	16.67
Main gear distance from nose	35.01	114.9
Main gear separation (spanwise)	9.75	32.0

Table 13: Tip-over angles from landing gear sizing and placement

Parameter	Constraint	Value
Lateral tip-over	$\geq 5°$	5.47°
Rotation clearance	$> 6.8°$	10.39°
Longitudinal tip-over	$\geq 15°$	29.87°
Nose-to-main tip-over	$\leq 55°$	41.04°

8.9 Retraction Mechanism

The landing gear retraction mechanisms are depicted in Figure 19. The red and blue lines represent two different hydraulic actuators and the green line is a pinned support, while the black line represents the actual landing gear strut.The actuators change length to adjust the position of the landing gear. The landing gear are in locked positions if the hydraulic actuators are fully deployed

or retracted. Figures 20 and 21 show the aircraft in side and bottom views with the landing gear retracted.

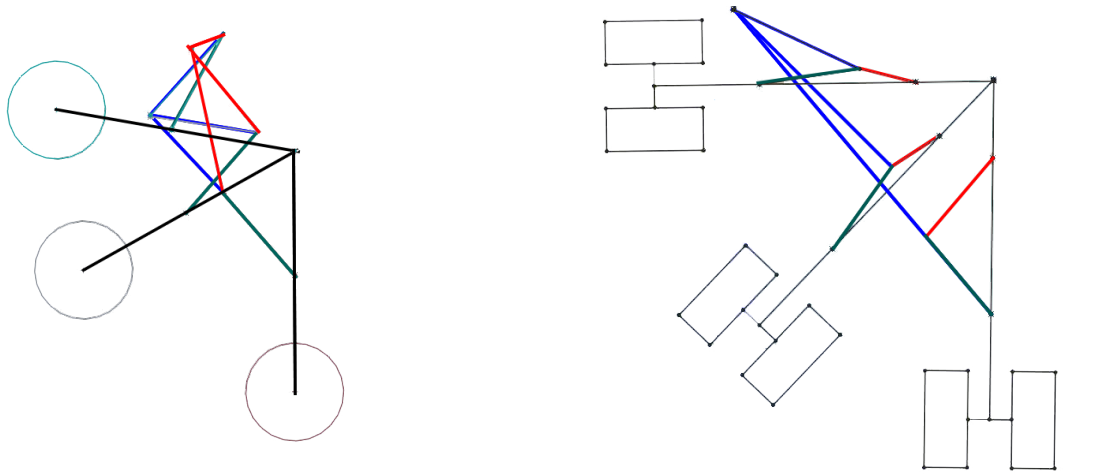

(a) Nose gear retraction mechanism

(b) Main gear retraction mechanism

Figure 19: The nose and main landing gear retraction mechanisms

9 Method Validation

In order to assess the validity of our code we ran it with the physical parameters of a 737-800 to check the sizing against that of the real 737-800. We chose the 737-800 because the AVL webpage contained an example geometry file using this aircraft. This allowed us to use this AVL geometry file, eliminating the need to rewrite our AVL geometry generator function to model the 737-800. However, in order to attain even greater fidelity, we found a NASA paper detailing efforts to improve the lift-to-drag ratio of a single-aisle transport aircraft [9] that listed the lift-to-drag ratio of the 737-800 as 15 for its cruise Mach number of 0.785. This allowed us to hard-code a lift-to-drag ratio of 15 into our cruise fuel fraction function. We still needed K for other functions however; so, we used AVL to calculate K by running three points with the 737 geometry file at cruise conditions and fitting a parabola. We then hard-coded the K value we found, 0.038, into the program. Finally, we hard-coded the thrust loading in as well to avoid any uncertainty about which design constraints were in effect. With these modifications, our code was able to match the real 737 to within a

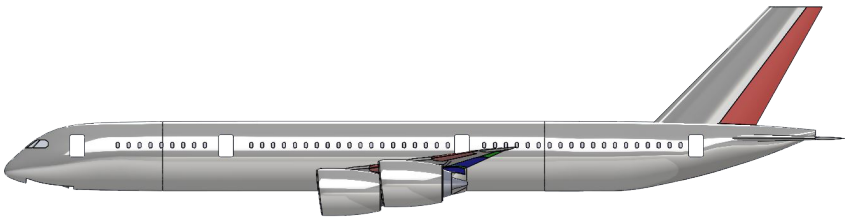

Figure 20: Landing gear retraction, side view

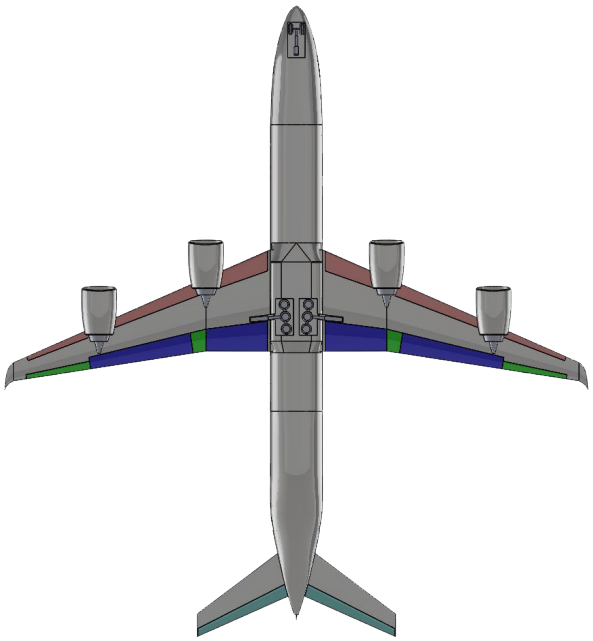

Figure 21: Landing gear retraction, bottom view

reasonable margin on all major outputs. Table 14 shows the results of our validation.

Table 14: Validation of design code

Parameter	Real 737-800	Design Code	Percentage Difference
Takeoff Weight, kg (lbs)	79,016 (174,200)	83,071 (183,140)	5.13
Empty Weight, kg (lbs)	41,413 (91,300)	35,997 (79,359)	-13.1
Fuel Fraction	0.2648	0.3041	12.9
Takeoff Thrust, kN (lbf)	242.9 (54,600)	255.3 (57,402)	5.13
Engine Weight, kg (lb)	2,366 (5,216)	2,507 (5,526)	5.9

10 Cash Operating Cost

To effectively understand the airplane's budget, and limits set on it, an analysis was conducted to estimate the cash operating cost (COC) of the airplane. These costs are the ones directly associated with the flight of the airplane, including crew and pilot costs, fuel, and maintenance of the aircraft.

An important factor in estimating these expenses is the Cost Escalation Factor (CEF), which is utilized in determining costs given a base year and the year in which the flight will occur (e.g. 2025), escalating accordingly,

$$CEF = t_{CEF}/b_{CEF} \tag{31}$$

where t_{CEF} and b_{CEF} are calculated by the following relations based on the year 2006:

$$t_{CEF} = 5.17053 + .104981(t_{year} - 2006) \tag{32}$$

$$b_{CEF} = 5.17053 + .104981(b_{year} - 2006) \tag{33}$$

Most of the cost estimations for such things as crew and fuel costs are determined by the estimated block time t_b as well as maximum takeoff weight (MTOW) and fuel weight. Block time is the overall time that an aircraft is in use for a given flight, in our simplified case from takeoff to landing of our plane. An estimation of airspeed and distances gave our team a block time of 18.12 hours, from which crew and fuel costs were able to be calculated as seen in Table 15 below. Missing from the table are oil costs, which were assumed to be zero - as specified in the design requirements.

Table 15: Results of Cash Operating Cost Estimation

Parameter	Cost (USD)
Crew	81,739
Attendants	16,552
Fuel	239,163
Airport fees	692
Navigation fees	1,732
Airframe Maintenance	73,004
Engine Maintenance	10,130
COC	423,013
COC/pax-nmi	0.40846
COC/pax, USD	3,384.09

Looking at what each parameter relies on gives a clearer view into what drives our design, and why certain values are lower than some of our competitors. For example, our crew costs rely mostly on MTOW, which matches up with our rather small takeoff weight. Our biggest value comes from our fuel cost, which is reduced by both more efficient engines (in terms of burn rate) and lower takeoff weight, explaining why that estimation is on the lower side as well. With our current COC analysis, our cost per passenger is $3,384, creating a margin for profitability for our plane. The COC was minimized using a gradient-based optimization, as described in the following sections.

11 Multidisciplinary Design Optimization Overview

The most critical part of our design process was the Multidisciplinary Design Optimization. All of the design variables involved in this project are so closely intertwined that it is nearly impossible to judge the impact of changing just one, let alone reach an optimal design without the use of an optimizer. Even more importantly, the set of constraints the plane must satisfy are also closely intertwined, and finding a design that satisfies all of them is no small feat. Thus trying to optimize a design while also satisfying the constraints requires the use of an optimizer. For this reason, our code was designed to be compatible with Matlab's `fmincon` function, and it evaluates all of the constrained parameters within the code. This allowed us to run the optimizer as described below and produce a plane that was nearly completely designed, meeting all constraints at the minimum cash operating cost.

11.1 Choice of Variables

One of the most important decisions regarding optimization was the design variables with respect to which we would optimize. The obvious ones are the wing planform variables: reference area, span, taper ratio, and sweep angle. Those four variables define the wing geometry in its entirety. The aspect ratio is the real parameter of interest when it comes to wing efficiency, but because our bound in that regard is with respect to the maximum gate span of 80 meters, we used span as our variable so that we could more easily bound it, and let the program determine the best aspect ratio indirectly. In addition, our experience leading up to the preliminary design review showed us how important the wing leading edge position was in determining both the static margin, which greatly impacts trim drag and thus lift-to-drag ratio, and also the tipover angles, so it was clear that the position of the wing leading edge should also be an input to the optimization. Choosing the other variables with respect to which to optimize was more difficult. We knew that the more variables we used, the longer the optimization would take, and we anticipated having a need for multiple runs to find the best value, so we couldn't afford for it to take an exorbitant amount of time to run. Thus we needed to limit our variables to only the most important. Another lesson we had learned from preparing for the preliminary design review was that the maximum landing weight as a fraction of maximum takeoff weight has a large impact on the final design because the balked landing climb thrust loading constraint is one of the most restrictive, and it is directly proportional to the maximum landing weight. For this reason we chose the maximum landing weight as a fraction of takeoff weight to be our sixth and final design variable for the optimization. We also considered the tail volume coefficient and geometric parameters, but the volume coefficient method was working well and thus those variables were deemed too computationally expensive for the minimal benefit.

11.2 Bounds and Starting Point

Once we had selected our variables, we set up our code to take them as inputs. Another important aspect of our optimization setup was the bounds we set on these variables. For our first attempts, we set the bounds as wide as possible, hoping to find the best point. However, this would lead to problems in the process, because the optimizer would often try various combinations of extreme values that were so unusual as to crash AVL. For example, the optimizer would often try to put the wing as far back as possible with the longest span possible on its first iteration, and this would put the mean aerodynamic center behind the horizontal stabilizer because of the sweep. That would cause our tail sizing functions to output negative reference areas, which would then cause trouble in AVL. Another common error was for the optimizer to place the wing such that the moment arm between the wing and the tail was very small, leading to very large tail reference areas, in the thousands of feet. This would also cause problems in AVL. The result of this early troubleshooting was that we tightened our bounds to keep the optimizer in a safe design space. The resulting ranges are shown in Table 16.

During the vetting of our optimization code we found that the use of AVL is very important. Finding both the trim drag and the correct correlation between wing planform and aerodynamic performance is only possible using AVL. If we used the simplified equation for K involving aspect ratio and Oswald efficiency factor in order to calculate the drag in flight, the effect of large aspect ratios is greatly overestimated, which leads the optimizer to return a plane with as long a span as possible. Furthermore, the effects of static margin and trim drag are not accounted for, meaning that the optimizer would try to put the wing as far forward as possible, for reasons not entirely clear. Thus although using AVL significantly slows down the process, it is critical to obtaining

accurate results. Closely coupled to this, calculation of the center of gravity in each run to be input into AVL is extremely important in calculating the trim drag.

The final key component of a successful optimization run is the starting point. We found that it is important to have a starting point that meets all of the constraints because otherwise the optimizer may not find its way into the feasible region, but instead find a minimum that is infeasible. Further, because of the gradient based nature of `fmincon`, it will find the local minimum but that might not be the global minimum. For this reason it was important to use multiple starting points, and also to confirm the optimality of our results using trade studies, as described in Section 12.3. Finding good starting points was one of the most time consuming parts of the optimization, other than actually running the optimizer, because before we ran the trade studies it required simply educated guessing and small changes to the design variables. In future work it might be beneficial to run low-resolution trade studies first to determine the trends, and then choose a feasible starting point near the global minimum and use `fmincon` to find the optimal point.

12 Design Refinement

In order to obtain a design for the aircraft that truly minimizes the objective function, subject to the constraints on the design, we turn to the powerful gradient-based optimization that `fmincon` utilizes. By specifying the objective (operating cost), the bounds and nonlinear constraints on the design variables, and a reasonable starting "guess" for the design, `fmincon` will iteratively search the design space for the optimal design. The following sections describe the design variables that are allowed to change in the iterations, the constraints on the design, and the calculation of the objective function.

12.1 Design variables

The constraints on the design parameters involved in the optimization procedure are divided into input bounds and output constraints, as outlined in Table 16. As mentioned above, these constraints are set to be relatively strict in order to ensure that the optimizer does not attempt any unusual design that might crash the program. This is especially important for the span, sweep, and wing leading edge position constraints, which can combine to put the mean aerodynamic center behind the tail. The lower bound of the sweep was set to 23.7° because we learned from our airfoil research that we needed a perpendicular Mach number of 0.76 or less to ensure Mach drag divergence would not occur, and given our cruise Mach number of 0.83, this is the angle required to enforce that necessity. The 35° maximum on sweep, 240 foot maximum on span, and 120 ft maximum on wing leading edge were chosen to keep the mean aerodynamic center ahead of the horizontal stabilizer. The maximum landing weight as a fraction of takeoff weight minimum bound is set to 0.65 based on historical data in the lecture slides, and 1 is the largest value possible for that parameter. The wing loading constraint is calculated based on the landing constraint set in the FAR, calculated for each specific design in our code. If this maximum wing loading is too high to be structurally feasible, our code resets it to 170 lb/ft^2, based on the maximum wing loading found in current transport aircraft, 173 lb/ft^2 on the MD-11F. However, our code inputs the fixed wing area and calculates a weight, meaning we must constrain the wing loading externally to ensure it exceeds neither the FAR maximum nor the structural maximum. The static margin must be positive to have a statically stable aircraft, but must also not be too large or the aircraft will not have have sufficient elevator authority to pitch up enough to land. The 0.4 maximum was set based on the range given by Martins [6]. Finally, the 15° minimum on longitudinal tipover angle is set to comply with the FAR. The other FAR angle requirements are all met within the code itself by setting the

landing gear height at the minimum required to achieve them, and then the longitudinal tipover angle is constrained as an output to ensure the landing gear height is not too tall to satisfy that constraint. Our landing gear placement within the code is conservative, placing the landing gear slightly forward of the flap to allow room for the structure to carry the landing gear even though this reduces the longitudinal tipover angle. In postprocessing the results we are able to move the landing gear back once the actual structure is sized, increasing the margin on the longitudinal tipover angle. Thus the optimizer outputs an angle close to 15° , but our final longitudinal tipover angle is 29.87° with the aft-most center of gravity possible.

Table 16: Design parameter constraints

	Parameter	Symbol	Constraint
Design Variables	Wing reference area	S_{ref}	$2900 \leq S_{ref} \leq 4000$ ft^2
	Wing span	b	$160 \leq b \leq 240$ ft
	Wing taper ratio	λ_{wing}	$0.2 \leq \lambda_{wing} \leq 0.6$
	Wing LE distance from nose	x_{wingLE}	$70 \leq x_{wingLE} \leq 120$ ft
	Wing sweep angle	Λ	$23.7° \leq \Lambda \leq 35°$
	Max landing weight ratio	W_{land}/W_{TO}	$0.65 \leq W_{land}/W_{TO} \leq 1.00$
Calculated Constraints	Wing loading	W/S	$W/S \leq (W/S)_{max}$
	Static margin	SM	$0 \leq SM \leq 0.4$
	Longitudinal tip-over angle	φ_{long}	$15° \leq \varphi_{long}$

These ranges are enforced in the context of `fmincon` by specifying upper and lower bounds on the inputs and by providing a nonlinear constraints function which contains the constraints on certain parameters calculated in the process of evaluating the objective function value. The structure of a typical run of `fmincon` in Matlab is as follows:

[$\mathbf{x}^*$,COC] = `fmincon`(`@objective`, $\mathbf{x}^0$, [ ], [ ], [ ], [ ], **lb**, **ub**, `@nonlin_constraints`),

where [COC] = `objective`($\mathbf{x}$)
and [$\mathbf{c}$, $\mathbf{c}_{eq}$] = `nonlin_constraints`($\mathbf{x}$)

$$\mathbf{x} = \left[S_{ref}, \quad b, \quad \lambda_{wing}, \quad x_{wingLE}, \quad \Lambda, \quad W_{land}/W_{TO}\right]$$
$$\mathbf{c} = \left[(W/S - (W/S)_{max}), \quad -SM, \quad SM - 0.4, \quad (15° - \varphi_{long})\right] \leq \mathbf{0}$$
$$\mathbf{c}_{eq} = \left[\ \right] = \mathbf{0}$$

The key to our ability to constrain parameters calculated within the design program is in the declaration of global variables in the context of the program's highest level. Because the function which evaluates the objective function value can only output COC (as it is the only variable being minimized), the design program would normally need to be run twice for each set of input variables: once for the evaluation of the objective function and once for the evaluation of the nonlinear constraints. However, by using global variables within the design program, certain values calculated as intermediate steps toward evaluating the objective function can be stored in a space that can be accessed by the nonlinear constraints function.

12.2 Optimized solution

From the `fmincon` optimization, a design point for the aircraft was found. An important factor in the convergence of the iterations to a feasible solution was the choice of the starting point for the optimization $\mathbf{x}^0$. We found that supplying a starting point with all of the input variables within their bounds was not enough to guarantee the success of `fmincon`; rather, the result of the starting point had to also satisfy all of the constraints. Further, because of the gradient-based nature of the optimizer, it is susceptible to finding local minimums rather than global minimums. For this reason, we used several starting points, and confirmed our results with a trade study. Table 17 shows the chosen starting point for the optimization and the converged solution, both satisfying the constraints on the input and output variables. Although the design variables did not change drastically, the optimization did reduce the COC by a relatively large amount, from \$428,900 at the starting point to \$423,013 at the converged design point, an improvement of \$5,887. This primarily shows the large impact static margin has on cash operating cost. The optimizer frequently attempted to make the static margin as large as possible within the constraints. This seems to indicate that there is an aerodynamic benefit in cruise from having a static margin greater than 0.4, but we needed to constrain it to ensure that our airplane could safely land. Additionally, the optimizer took 5 iterations and 153 function evaluations to reach the final point, as shown in Figure 22b. This is nearly as many function evaluations as the optimization for the critical design review presentation, which took 12 iterations and 175 function evaluations while making major changes to the design. That plot can be seen in Figure 22a. Table 18 shows a few of our other starting points and the points returned by `fmincon`.

Table 17: Result of `fmincon` optimization

	Starting point, $\mathbf{x}^0$	Parameter	Converged point, $\mathbf{x}^*$	Bounds
Design Variables	3,800 ft^2	S_{ref}	3,800.5 ft^2	$2900 \leq S_{ref} \leq 4000$ ft^2
	188 ft	b	187.99 ft	$170 \leq b \leq 240$ ft
	0.2	λ_{wing}	0.2	$0.2 \leq \lambda_{wing} \leq 0.6$
	89 ft	x_{wingLE}	89.3 ft	$70 \leq x_{wingLE} \leq 120$ ft
	23.7°	Λ	23.74°	$23.7° \leq \Lambda \leq 35°$
	0.7305	W_{land}/W_{TO}	0.7305	$0.65 \leq W_{land}/W_{TO} \leq 1.00$
Calculated Constraints	151.2 lb/ft^2	W/S	148.74 lb/ft^2	$W/S \leq (W/S)_{max}$
	0.3963	SM	0.3999	$0 \leq SM \leq 0.4$
	16.0°	φ_{long}	16.18°	$15° \leq \varphi_{long}$

These points show the extent to which `fmincon` was constrained. The starting point was of utmost importance, because as can be seen, the optimizer often cannot move far without violating constraints. It takes a great deal of effort to find starting points that meet all of the constraints, and being limited by time, these were the points we were able to run. This was in contrast to the optimization run prior to the critical design review presentation in which the optimizer changed all but one of the design variables by a fairly large amount. Interestingly, though, while the optimizer did not move our design point much in our most recent optimization, it still found a point with a cash operating cost \$6,810 lower than the optimization for the presentation. Our trade studies also verified that our chosen point was in fact a global minimum.

Point 3 shows the result when the starting point does not meet all of the constraints. That point was used as an experiment, as even the input did not meet the longitudinal tipover angle

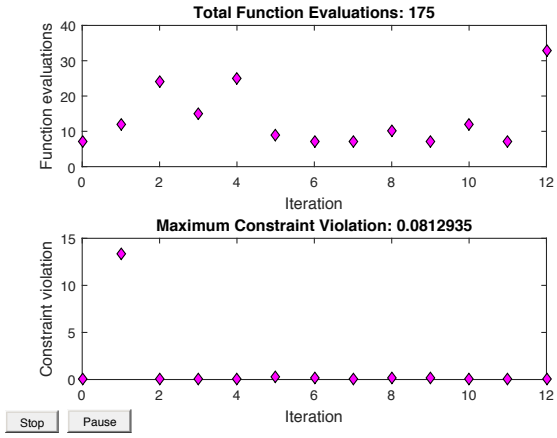

(a) Plot showing convergence of optimization for critical design review presentation

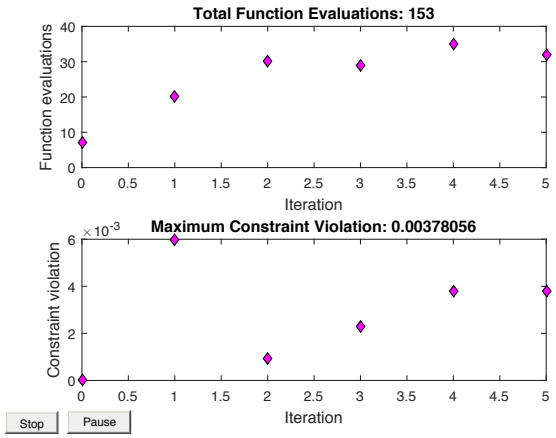

(b) Plot showing convergence of final optimization

Figure 22: Convergence of designs through `fmincon` optimization

Table 18: Result of `fmincon` optimization for other starting points

Parameter	In 1	Out 1	In 2	Out 2	In 3	Out 3	In 4	Out 4	In 5	Out 5
S_{ref} (ft^2)	3,800	3,801	3,900	3,900	3,500	3,799.9	3,300	3,305	3,700	3,717
b (ft)	188	187.9	170	169.9	200	181.1	190	189.9	175	174.1
λ	0.2	0.2	0.2	0.2	0.5	0.2088	0.2	0.2	0.22	0.225
x_{wingLE} (ft)	89	89.3	90	90	95	80.2	92	92.3	84	88.4
Λ (rad)	23.7	23.74	25.78	25.73	28.64	23.74	23.74	23.74	24.64	24.58
W_{land}/W_{TO}	0.731	0.731	0.731	0.731	0.8	0.789	0.731	0.732	0.670	0.669
W/S (lb/ft^2)		149		182		144.6		154		158
SM		0.399		0.375		0.25		0.51		0.377
φ_{long} (°)		16.2		21.5		6.58		15.6		17.4
COC (USD)		423,013		501,000		414,000		398,000		442,000

requirement. However, we see that given the freedom of not being within one of the constraints, the optimizer moved a great deal more than for other points, but it could not find its way back into the constrained region. The final longitudinal tipover angle for this point is only 6.58°, well below the minimum of 15°, but the optimizer did find a point with a reduced cash operating cost of $398,000 without meeting that constraint. This run confirmed that the optimizer was functioning properly, because it changed the design variables to find a minimum. It also provided us with important information because it showed that 3,800 square feet of wing area, our final design choice, minimized cash operating cost. Finally, the sweep angle was reduced from 28.6°to 23.7°, the lower bound, showing that even accounting for wave drag, a minimum sweep angle will minimize cash operating cost because of the lower wing weight it affords. With point 2 we used a starting point with a wing loading above 180 lb/ft^2 to test the optimizer, as it would usually reduce the wing loading in the course of an optimization. However, the optimizer did not reduce the wing loading, and as with several of the other runs, it returned a point very close to the starting point.

12.3 Trade studies

In order to verify that the point chosen by `fmincon` is truly an optimal design point, the design space around the point was explored by varying the design parameters that most strongly affect the feasibility around that point. To do this, the design program was run for several incremental combinations of wing span b and wing leading edge distance from the nose x_{wingLE} (keeping the remaining design variables constant) such that the objective function could be plotted as a function of these two variables. Figures 23a to 23d show contours of the objective function (COC) as well as the static margin, wing loading, and longitudinal tip-over angle to demonstrate that the design point chosen by `fmincon` minimizes the COC subject to the constraints on these parameters.

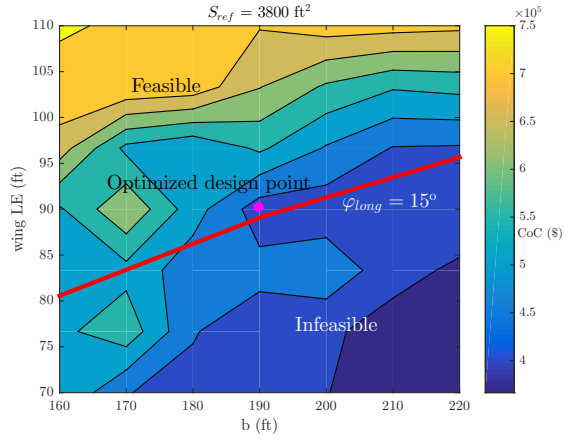

(a) Cash operating cost (COC) variation around design point shows minimization of objective while satisfying tip-over constraint

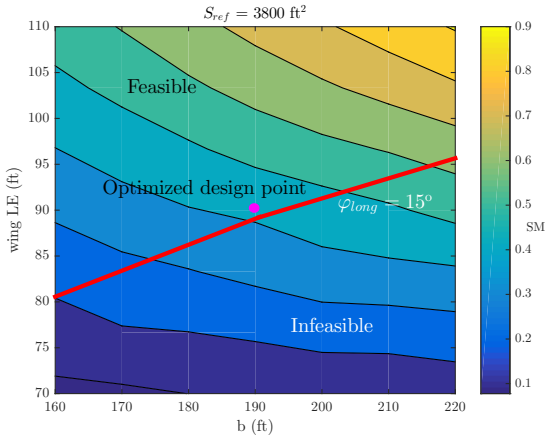

(b) Static margin (SM) of design point satisfies specified constraint of less than 0.4

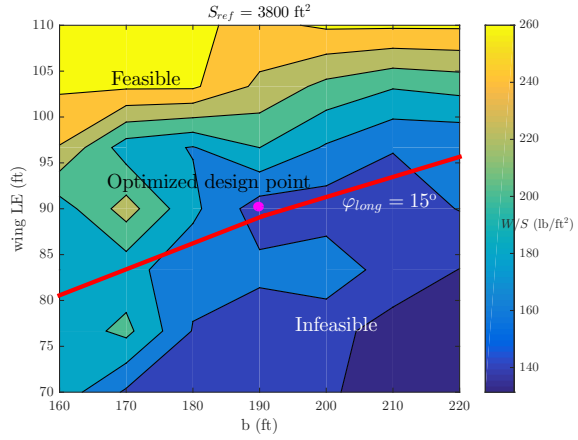

(c) Wing loading (W/S) variation around design point satisfies $(W/S)_{max}$ constraint

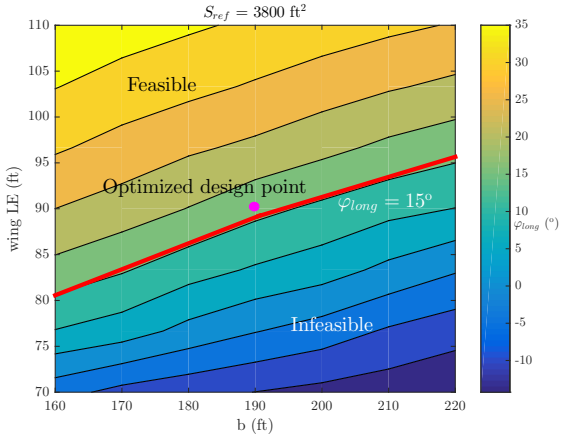

(d) Longitudinal tip-over angle (φ_{long}) for design point satisfies constraint of greater than 15°

Figure 23: Trade studies of design output variables by variation of input variables around `fmincon`-optimized point confirm validity of optimization and feasibility of converged design point

13 Structures

13.1 Lift Distribution

The distribution of the lift on the wing in our cruise condition can be seen in Figure 24. The lift can be seen to be roughly constant over the Yehudi break, and then decrease steadily in the spanwise direction approaching the tip. Our wing box should be sufficient to handle these lifting loads. Having four engines also relieves the lifting load on the wing by providing weight at two locations to counteract the lift.

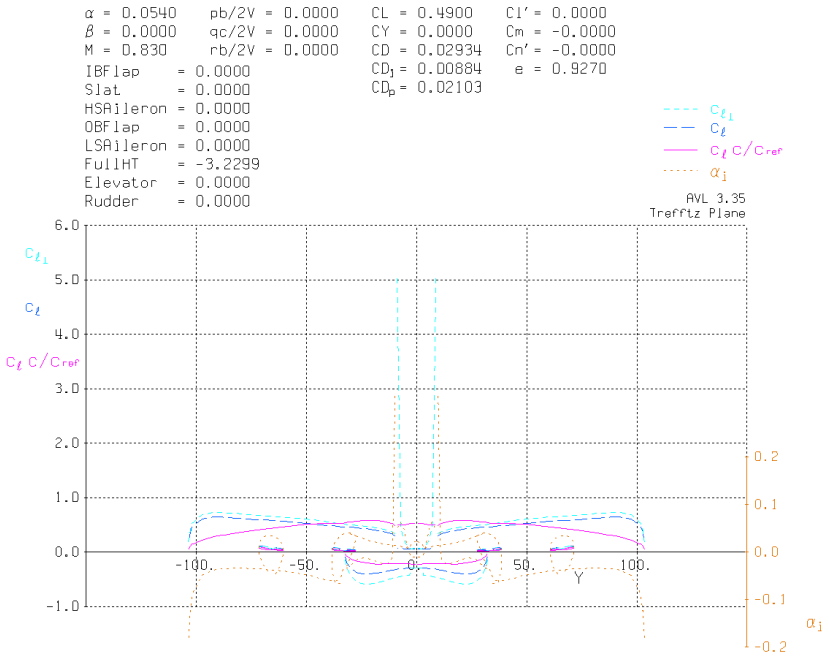

Figure 24: Cruise condition lift distribution

13.2 V-n diagrams

The flight envelope of our conceptual aircraft is visualized by the V-n diagrams. They are made of a combination of maneuver diagram and gust envelope.

The maneuver diagram shows the variation in load factor with airspeed for maneuvers. The positive and negative maximum maneuver load factor are chosen as +2.5 and -1.0 respectively. This range is general for airplanes weighing more than 50,000 lbs. At low speed, the maximum load factor is constrained by the aircraft maximum C'_N (25% higher than maximum C_L due to uncertainties in dynamic stall). The intersection of this stall-curve and the maximum load factor line defines the point of design maneuver speed, V_A. Beyond the V_A, full deflections of control devices are not permitted because of the load factor limit. The maximum operating speed, V_{MO}, is set to be 6% higher than the maximum design cruise speed, V_C. Meanwhile, the design dive speed, V_D, is set to be 7% higher than V_{MO}.

The gust envelope indicates the load associated with vertical gust over the range of speeds associated with the maneuver diagram. The loads due to vertical gusts can be calculated based on this expression given in FAR Part 25,

$$n = 1 + \frac{K_g C_{L_\alpha} U_e V_{EAS}}{498 W/S}, \tag{34}$$

$$where \quad K_g = \frac{0.88\mu}{5.3 + \mu}, \quad \mu = \frac{2(W/S)}{\rho \bar{c} C_{L_\alpha} g} \tag{35}$$

The magnitude of the vertical gust at a particular altitude and airspeed is specified by the FAA based on statistical observations. In the gust envelope, the gusts associated with V_B, V_C, and V_D are considered. V_B is the velocity associated with rough air gust, which is the point of intersection of the stall-curve (maximum C_L is used for gust related calculations) and the rough air load factor line.

The diagram on the left is the V-n diagram for minimum weight. The diagram on the right is the V-n diagram for maximum weight. The colored lines represent the gust load envelope. The black lines represent the maneuver load envelope. The solid lines define the boundaries of the gust-maneuver combined V-n diagram.

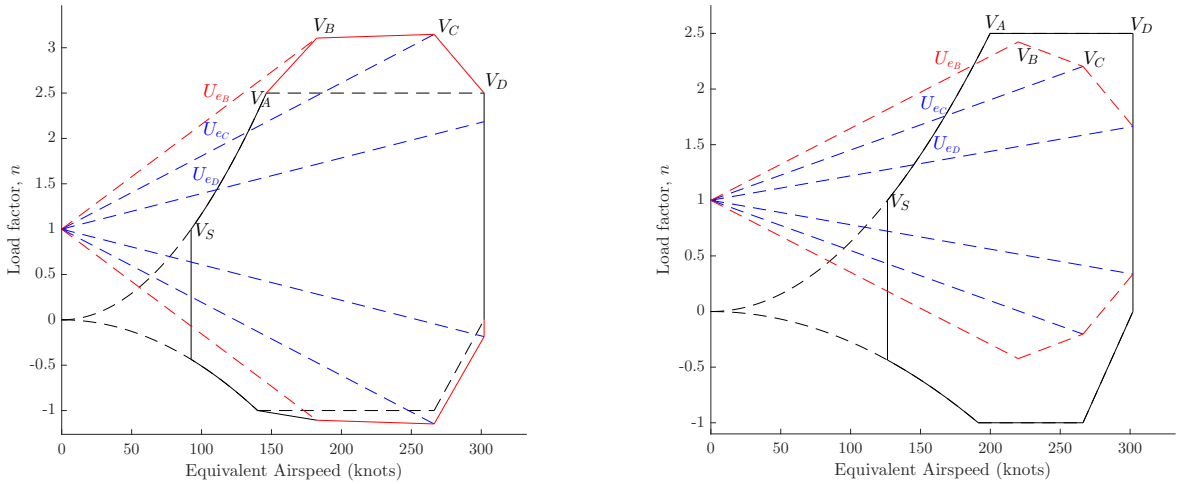

(a) V-n diagram for minimum weight (303,060 lbs) (b) V-n diagram for maximum weight (565,280 lbs)

Figure 25: V-n diagrams

The design speeds, the vertical gust speeds, and the associated limit loads for the maximum and minimum weights are tabulated as below:

Table 19: V-n diagram loads and velocities for minimum weight (303,060 lbs)

Design speed name	EAS magnitude [knots]	Vertical gust speed [m/s (ft/s)]	Limiting profile	Limit load magnitude
V_A	146.31	-	Maneuver	2.5
V_B	182.35	16.15 (53)	Gust	3.11
V_C	266.29	11.28 (37)	Gust	3.15
V_D	302.03	5.49 (18)	Maneuver	2.5

Table 20: V-n diagram loads and velocities for maximum weight (565,280 lbs)

Design speed name	EAS magnitude [knots]	Vertical gust speed [m/s (ft/s)]	Limiting profile	Limit load magnitude
V_A	199.83	-	Maneuver	2.5
V_B	219.97	16.15 (53)	Maneuver	2.5
V_C	266.29	11.28 (37)	Maneuver	2.5
V_D	302.03	5.49 (18)	Maneuver	2.5

14 Structural Design

For our aircraft, we must consider the structure that holds it together. This structure adds weight to the overall design of the aircraft, and thus increases the cost. The aircraft experiences loads that include lifting loads on the wings, forces and torsional loads due to the engines, and loads from the aircraft's weight. These loads are taken into consideration, and the structure is built to support the loads that are determined from analysis, and from the configurations that are used in comparable passenger aircraft.

14.1 Load Paths

There are many loads that the aircraft experiences, which range from the loads induced by flight, loads from its own weight, and loads that are from contact with the ground through the landing gear and the weight of the four engines. The load-path of the loads that are present are shown in Figure 26.

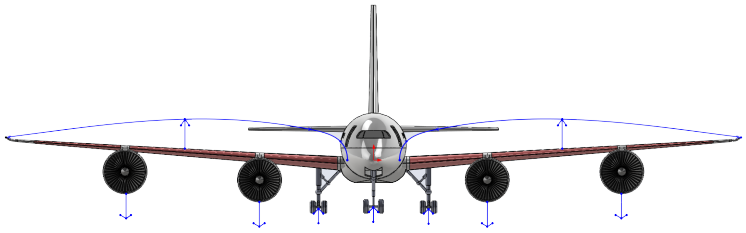

Figure 26: Distribution of main loads on aircraft

The point loads produce high stress concentrations that need to be distributed through the entire structure to effectively dissipate the stresses caused by the loads. For the distributed loads, the stress needs to be distributed along a single structure that attaches to the fuselage to transfer some of the load there to prevent significant deflection of the wings.

14.2 Fuselage

The structure of the aircraft fuselage is shown in Figure 27 and Figure 28.

The aircraft utilizes a combination of structural elements. The surrounding material is a skin, which carries vertical, lateral, and torsional loads. Longerons are used for longitudinal support due to loads from pressurization, while at the same time helping the skin carry the longitudinal tension and compression loads. Finally the frame is used to maintain the shape of the fuselage,

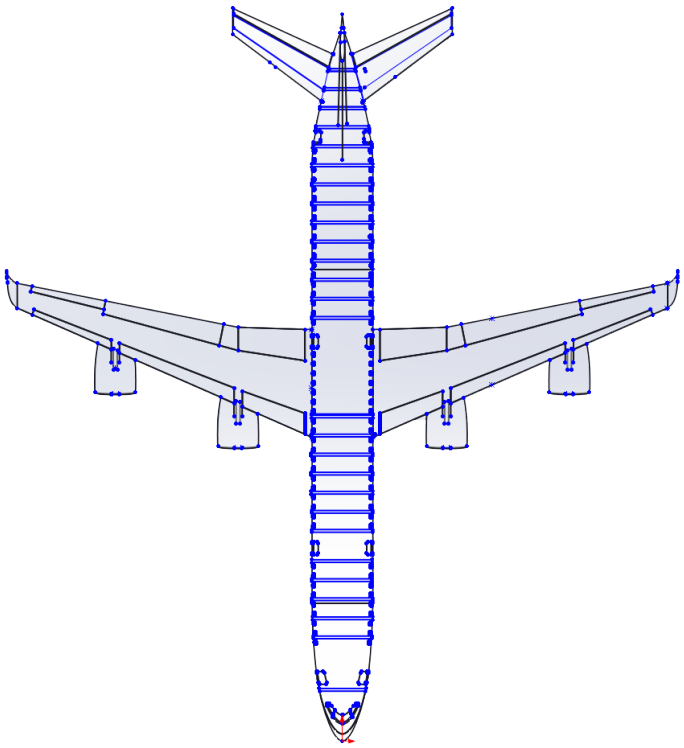

Figure 27: Top view of the fuselage structure

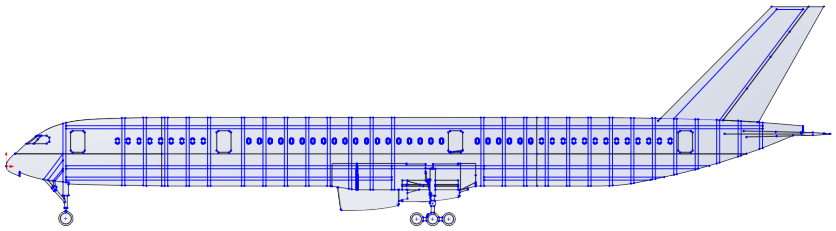

Figure 28: Side View of the fuselage structure

while reducing the effects of buckling and providing attachment points for other structures, such as wings, horizontal and vertical stabilizers, and landing gear.

14.3 Wings

The wings are supported with a wing box that goes through the center of the fuselage to both ends of the wings. There is also a kick spar that provides more structure to the wing and goes through the Yehudi break to the fuselage. The kick spar provides support for the main landing gear, and attaches to one of the longerons to distribute the load through the entire fuselage. The size of the box allows for the landing gear to be folded up and into the fuselage right behind it, while still allowing for fuel storage tanks to be placed at the center. The wing box is shown in Figure 29

below.

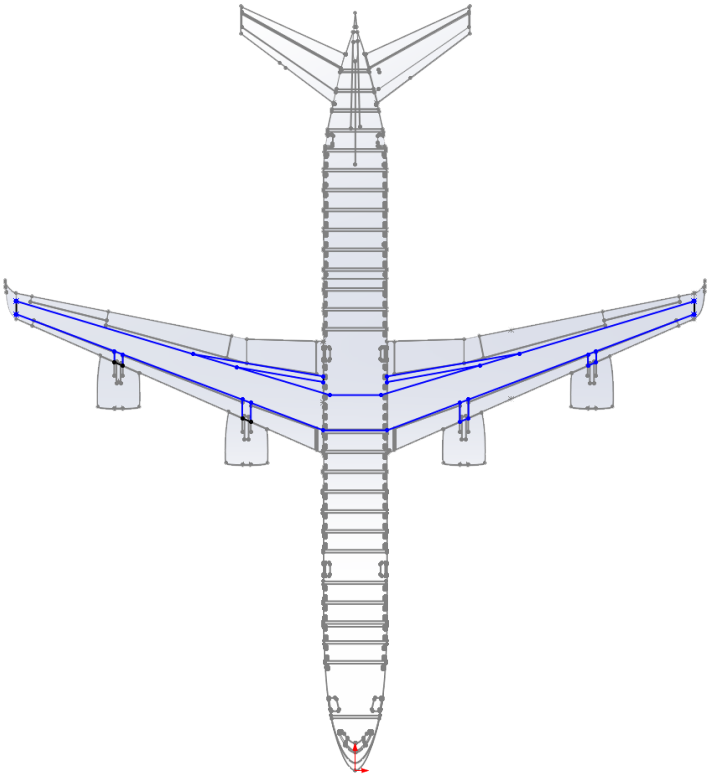

Figure 29: Top view of the wing box

The wing box was chosen to allow the fuel tank to go through the wings of the aircraft. To provide support, the box was surrounded by stiffeners on the inside of the boundary of the wing box. This would allow the airfoil to maintain its shape and reduce twisting of the wing due to distributed loads producing a moment along the length of the wing. The wing box is shown below in figure 30.

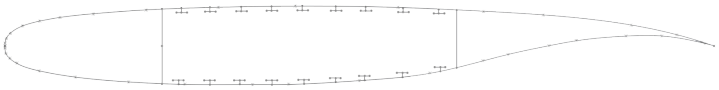

Figure 30: Side-view of wing box structure

15 Computational Framework

The most important aspect of our design process was the multi-disciplinary optimization. For this reason, our design code was organized to be compatible with an optimizer. It takes as input the design parameters we would optimize directly, including wing reference area, wing span, taper ratio, wing leading edge distance from nose, wing sweep angle, and maximum landing weight divided by

takeoff weight, and outputs the cash operating cost while also calculating various parameters that will be necessary in constraining the design. The choice of variable to optimize is describe in further detail in Section 11. Another important philosophy adopted in writing our code was to ensure that as many design constraints were enforced as possible. It was important to ensure that the optimizer could not exploit any unenforced constraint to lower the cash operating cost, as that could lead to an infeasible optimized design. For this reason, we needed a code that produced as complete a design as possible. The calculated parameters we constrained included static margin, tipover angles, wing loading, and rudder blanketing avoidance, in addition to the FAR requirements on thrust loading that are used in the sizing.

In order to calculate the cash operating cost, the code must calculate three major parameters: takeoff weight, fuel weight, and takeoff thrust. Each of these requires several more calculations. The takeoff weight is composed of the component weights, including the wing, fuselage, stabilizers, and landing gear, the fuel weight, the extra equipment weight, and the payload and crew weights. A more detailed analysis of our models for the component weights can be seen in Section 5. The takeoff thrust depends on the constraints set out in the FAR concerning landing, takeoff, climb, and cruise at various conditions. The thrust and weight are linked through these constraints, as the loading of the wing, in terms of takeoff weight divided by wing reference area, has an impact on the thrust needed to meet the constraints. This requires an iterative code to converge the values of both thrust and weight. In addition, although the weight of the structure depends in large part on the physical parameters, the updated weight models for the wing and fuselage also include the effect of the takeoff weight and limit loads, meaning that there must be an iterative loop within the weight calculator as well. The takeoff weight also has an impact on the fuel fraction, so this must be calculated within the iterative loop. Finally, the location of the center of gravity has a major impact on the takeoff weight because the wing leading edge position is fixed as an input parameter, as are the parameters defining the wing geometry and tail, meaning that the location of the neutral point is fixed. Thus, changing the center of gravity changes the static margin, changing the amount of trim drag and impacting the lift-to-drag ratio which has one of the largest sensitivities of any of the parameters, meaning a change in lift-to-drag ratio will have a major impact on the takeoff weight through the fuel weight, which will then change the component weights, moving the center of gravity again. This necessitated another iterative loop in order to converge the center of gravity position. This loop is by far the most computationally expensive because it requires running the Athena Vortex Lattice (AVL) aerodynamic solver to obtain the trim drag as a function of lift coefficient every time the loop is run, which is the bottleneck of our code in terms of computational time. Each run of AVL takes roughly 30 seconds, as required for accurate results. Our efforts to find the minimum time for accurate, robust use of AVL can are described in greater detail in Appendix A. We found that using manually distributed vortices among the sections of the lifting surfaces could ensure accuracy at significantly lower numbers of vortices, and thus significantly less computational time, while simultaneously ensuring that AVL would never crash when loading the file because of an inability to properly distribution the vortices among the sections. The entire rest of the code takes less than a second to run.

In addition to these nested convergence loops, there are several calculations that must be run once every time the code is run. We must calculate the wing planform geometry, such as the aspect ratio, root chord, mean aerodynamic chord (MAC), and MAC location given the inputs, as these depend solely on the geometry set by the inputs. We can then size the tail. Our tail sizing uses the volume coefficient method with volume coefficients for the vertical and horizontal stabilizers chosen from historical data. We know the location of the mean aerodynamic center of the wing from the wing geometry, and we place the stabilizers as far back as possible without impinging on the auxiliary power unit in order to maximize the moment arm between the wing aerodynamic

center and tail, as prescribed by the volume coefficient method. We also make a slight adjustment to the vertical tail location to ensure that at most two thirds of the rudder is blanketed by the flow from the horizontal stabilizer, as described in Section 6.1. This allows us to enforce yet another constraint within our code. The tail sizing functions use the volume coefficients to calculate the required surface area, and our chosen sweep, taper, and aspect ratios to define the entire geometry including the location of the mean aerodynamic center of each stabilizer.

We also use the component build-up method to generate the C_{D_0} of the aircraft, including the wave drag based on the sweep angle, as is described in Section 4.4. We must do this once each for cruise, takeoff, and landing conditions, as all three have not only different Mach numbers and ambient densities, but also drastically different profiles due to the deployment of flaps and landing gear. The inclusion of wave drag is important in order to ensure that our optimizer chooses the truly optimum wing sweep angle, balancing the drag reduction provided by sweep with the associated increase in wing weight. This is all of the preparation necessary to enter the convergence loops.

Following the weight convergence, the cash operating cost and final static margin are calculated, along with our final longitudinal tipover angle, which will be used as a constraint. In addition to calculating the center of gravity within each weight iteration loop, the code calculates the height of the landing gear required to meet the lateral tipover and rotation angle requirements. This height is a minimum, so the landing gear must be greater than that height. The longitudinal tipover angle sets a maximum on the landing gear height, which means that the height is bounded by these two values. To ensure that our design satisfies these requirements, we calculate the minimum height required to meet both the lateral tipover and rotation constraints, and then calculate the longitudinal tipover angle using that height so that it can serve as an external constraint in the optimization. The calculations involved in this process are described in further detail in Section 8.6.

Finally, our code includes a function that automatically generates a drag polar plot by iteratively running AVL using an iteration function similar to that used to find the equation for trim drag in the weight convergence loop. However, this function is much more extensive, running AVL at 20 different lift coefficients rather than the 3 used during the weight convergence loop, and processing the results to find the point at which either a section of the wing stalls or elevator deflection exceeds 20 degrees, marking the C_{Lmax}. Thus this function is left commented out during optimization, and is only run in the post-processing of the optimized results. The resulting drag polar can be seen in Figure 7. 15 (shown below) is a visualization of our MDO process, shown clearly and concisely using the XDSM (eXtended Design Structure Matrix) format, as presented by Lambe and Martins. [10]

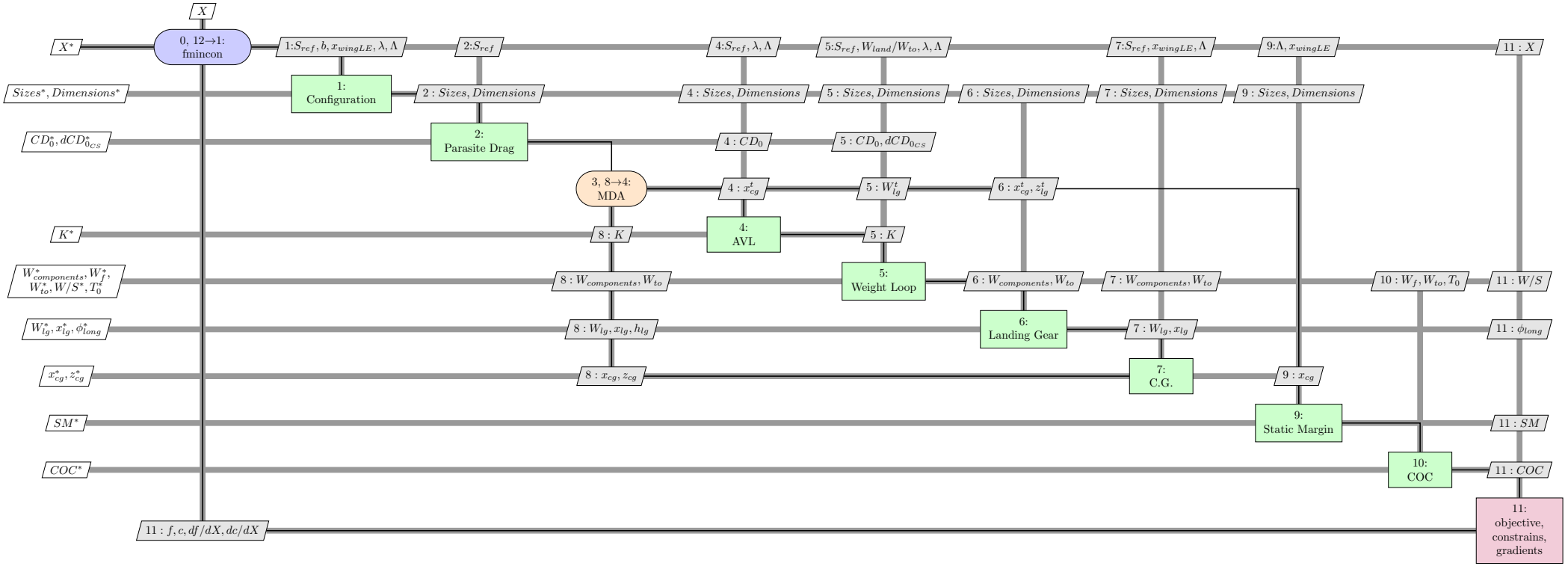
X
X^*
0, 12→1: fmincon
1:$S_{ref}, b, x_{wingLE}, \lambda, \Lambda$
2:S_{ref}
4:$S_{ref}, \lambda, \Lambda$
5:$S_{ref}, W_{land}/W_{to}, \lambda, \Lambda$
7:$S_{ref}, x_{wingLE}, \Lambda$
9:Λ, x_{wingLE}
11 : X
$Sizes^*, Dimensions^*$
1: Configuration
2 : $Sizes, Dimensions$
4 : $Sizes, Dimensions$
5 : $Sizes, Dimensions$
6 : $Sizes, Dimensions$
7 : $Sizes, Dimensions$
9 : $Sizes, Dimensions$
$CD_0^*, dCD_{0_{CS}}^*$
2: Parasite Drag
4 : CD_0
5 : $CD_0, dCD_{0_{CS}}$
3, 8→4: MDA
4 : x_{cg}^t
5 : W_{lg}^t
6 : x_{cg}^t, z_{lg}^t
K^*
8 : K
4: AVL
5 : K
$W_{components}^*, W_f^*, W_{to}^*, W/S^*, T_0^*$
8 : $W_{components}, W_{to}$
5: Weight Loop
6 : $W_{components}, W_{to}$
7 : $W_{components}, W_{to}$
10 : W_f, W_{to}, T_0
11 : W/S
$W_{lg}^*, x_{lg}^*, \phi_{long}^*$
8 : W_{lg}, x_{lg}, h_{lg}
6: Landing Gear
7 : W_{lg}, x_{lg}
11 : ϕ_{long}
x_{cg}^*, z_{cg}^*
8 : x_{cg}, z_{cg}
7: C.G.
9 : x_{cg}
SM^*
9: Static Margin
11 : SM
COC^*
10: COC
11 : COC
11 : $f, c, df/dX, dc/dX$
11: objective, constrains, gradients

The rectangles represent model analyses/components and the parallelograms represent the data inputs and outputs. Drivers, which are controlling iterative processes, are represented by rounded rectangles. Data connections are represented by think gray lines, while process connections are represented by thin black lines.

The operations corresponding to the numbers in the XDSM diagram are listed in Table 21.

Table 21: Operation processes of our MDO framework

0.	Pass initial values of the design variables to the optimizer.
1.	Use component "Configuration" to generate intermediate parameters related to sizing and dimensions.
2.	Compute parasite drag.
3.	Initiate the MDA (multidisciplinary analysis) for coupled analyses.
4.	Call AVL and generate the drag polars required.
5.	Execute the weight loop routine to generate weights.
6.	Determine landing gear sizing and placement.
7.	Compute the center of gravity.
8.	Check MDA convergence. If it has converged, continue; otherwise, return to 4.
9.	Compute the static margin.
10.	Calculate the cash operating cost.
11.	Evaluate objective and constraint function values.
12.	Compute new design state. If optimization has converged, return optimal solution; otherwise, return to 1.

16 Conclusions

16.1 Summary

Singapore Airlines wishes to resume their nonstop route from Newark to Singapore, and has reached out to our team Airbenders Ltd. to create an economically profitable, business class aircraft that still meets all of their requirements for their mission. With a cash operating cost of $423,013 (15), and parameters that exceed or meet all of the specifications set forth by our mission provider (1,2), our team believes our aircraft is a good fit for this flight. Our conventional tube and wing design lends itself to smart reductions and alterations in designs already in use, such as our takeoff weight of 256,407 kg (565,280 lbf) and a fuselage length of 223 feet, which allows for a very efficient aircraft.

Along with this, our team's optimization of our objective function (cash operating cost) was made possible by our software architecture. Constructing the software architecture to be compatible with the optimization tool provided by `fmincon`, we were able to minimize the COC by optimizing with respect to our chosen design variables while constraining it to meet all necessary requirements. In this manner, we found the wing planform variables and position of the wing that minimize the COC.

16.2 Feasibility of Design

Along with the mission given, our plane has to adhere to some specifications set by not only our customer, but the airports and runways it must takeoff and land from. This creates design drivers through analyzing which parameter can be made to have the smallest percentage of difference to the given requirement. In our plane's case, takeoff distance is our design driver, as shown below in Table 22. This is logical because fuel is our main payload, and would burn off before landing, making takeoff distance much larger than landing. As for gate span, our design was always comfortably within that range due to the small amount of passengers necessary for our flights, requiring nothing near the size of aircraft that would violate this requirement.

Table 22: Performance of aircraft against specifications

Aircraft Parameter	Value	Requirement	% Margin
Gate span, m (ft)	63.15 (207.2)	80 (262.5)	21.1
Maximum takeoff distance, m (ft)	3,353 (11,000)	3,353 (11,000)	0
Maximum landing distance, m (ft)	2,445 (8,023)	3,353 (11,000)	27.1

With this, our team believes that we have not only created a design that meets all requirements set by our customer, but one that is economically viable. It provides exceptional business-class amenities for its passengers, while still being capable of one of the longest commercial flights in the world at a competitive operating cost. Finally, we have provided room for future growth of the aircraft with the thrust margin that results from our choice of engines.

A AVL Vortex Validation

Prior to including AVL in our multi-disciplinary optimization, we needed to find a method for spacing the vortices on our surfaces in a robust way, to avoid crashing during the optimization. We also needed enough vortices to ensure accuracy. Finally, we wanted as few vortices as possible within the accurate range to minimize computational time, anticipating the large number of runs required for an optimization. The combination of these needs led us to perform an analysis on the impact of vortex spacing on AVL results and speed. This also proved to be a useful exercise in automating AVL.

We began with the 737 example available on the AVL webpage. The initial number of vortices present was 26 on each wing. To test the accuracy of this setup, we wrote a program to automatically run AVL and write the output to a file, and another program to read the file and record relevant information including the total C_L, total C_D, sectional C_l's along the span, Oswald efficiency factor, and control surface deflections. We then ran this at the same flight condition with numbers of vortices on each wing between 20 and 60 and plotted C_D as a function of number of vortices, as can be seen in Figure 31. We found that the C_D behaved erratically but the trend was that it decreased until roughly 60 vortices. This indicated that at least for the 737, we would need 60 vortices to ensure accuracy. In addition, we tracked the time required to run AVL for each number of vortices, and plotted that as well. The trend in that case was a nearly linear increase in computational time with number of vortices, as shown in Figure 32.

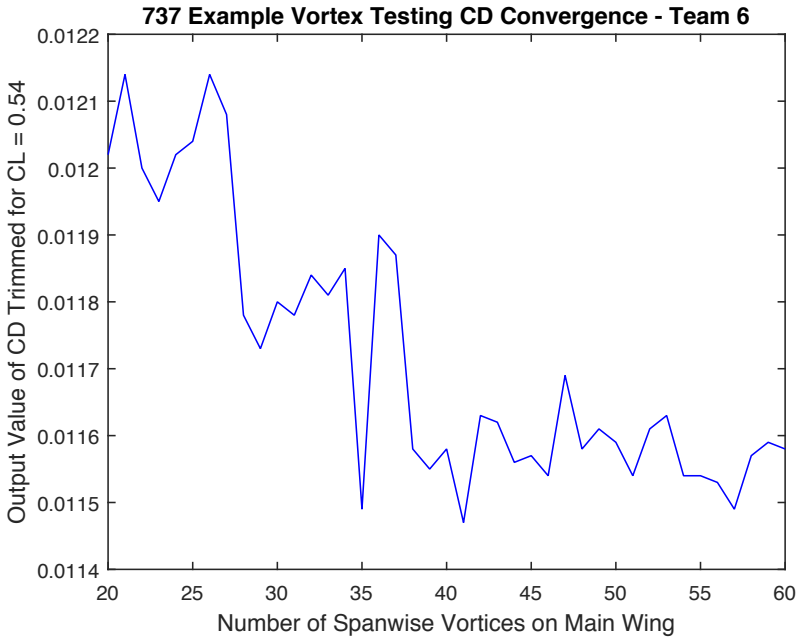

Figure 31: C_D decreases with number of vortices until around 60 vortices

We then began working with our own plane. We performed a similar analysis, iteratively running AVL using our code for numbers of vortices between 50 and 100 on each wing. We knew from earlier experience that using fewer than roughly 60 vortices would cause AVL to crash because it could not distribute the vortices among the 8 sections of our wing. This was a particularly bad failure mode because AVL would close itself so fast the warning could not be read, so finding the cause of this required capturing a picture of the screen in the split second that AVL was reading

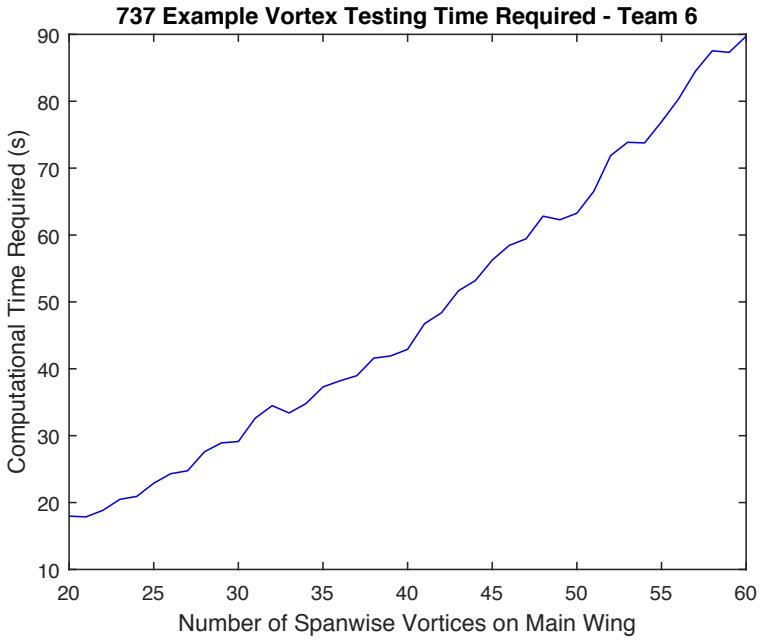

Figure 32: Computational time increases linearly with number of vortices

the file. The result of this study can be seen in Figure 33. The flat portions of the curve represent sections where AVL crashed, so the function read the output file written by the last run that didn't crash. Thus, we see that for our plane, accuracy does not depend on the number of vortices as long as there are enough to keep AVL from crashing, but it is not straightforward to predict whether or not AVL will crash based on number of vortices. The computational times required for these runs are shown in Figure 34. As before, the computational time increases almost linearly with number of vortices, but this time we see that it is nearly zero for the runs for which AVL crashed, confirming our conclusion that the flat portions of the C_D curve were a result of AVL crashing. The plot also shows the importance of minimizing the number of vortices in order to expedite our optimization, as a wing with 100 vortices on each side takes up to 90 seconds to run, and at least three runs are required to get the quadratic regression we need for calculating our lift-to-drag ratio.

Thus by experimentation we determined that at least 60 vortices per wing are required for accuracy, and we cannot accurately predict when AVL might crash as the wing geometry changes. This was unsatisfactory looking forward to an optimization process for which the shape of the wing would be highly variable and it would be critical that AVL work every time. Thus, we needed a different solution.

Reading the AVL user manual [11] we found that vortices can be defined for each wing section, as opposed to setting the number of vortices for the entire wing and letting AVL distribute them among the sections. This solves the problem of AVL crashing upon loading the geometry, because that was caused by the programs inability to properly distribute the vortices among the sections, so setting the number per each section ensures that there will be sufficient vortices in each section. Furthermore, setting the vortices for each section allows for distribution of more vortices where they are most needed, near abrupt changes in geometry, such as at flap edges, and in small sections, such as the one-foot section between the fuselage and the start of the inboard flap. This improves the accuracy of the solver as well. Setting the number for the wing as a whole limits the ways in which the vortices can be distributed, because there are only a few options for distribution: linear,

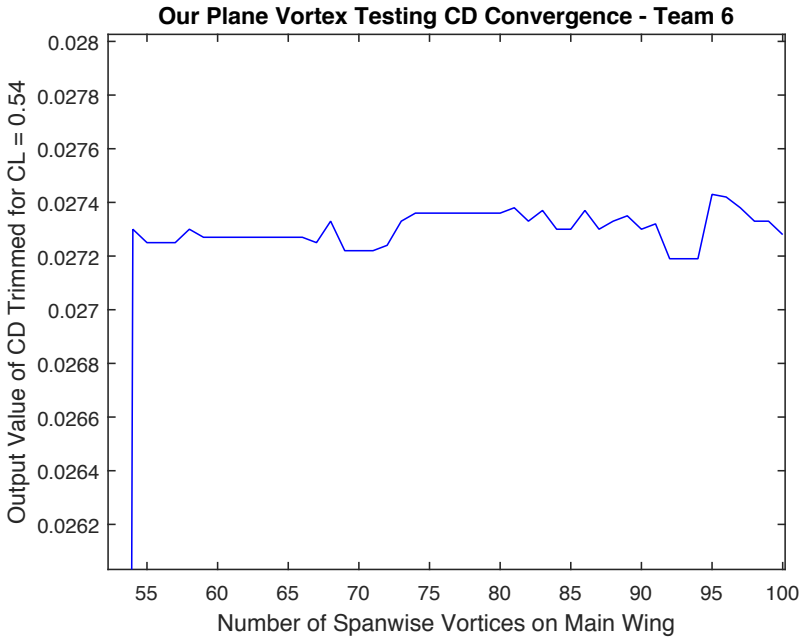

Figure 33: C_D remains nearly constant for all numbers of vortices that do not crash AVL

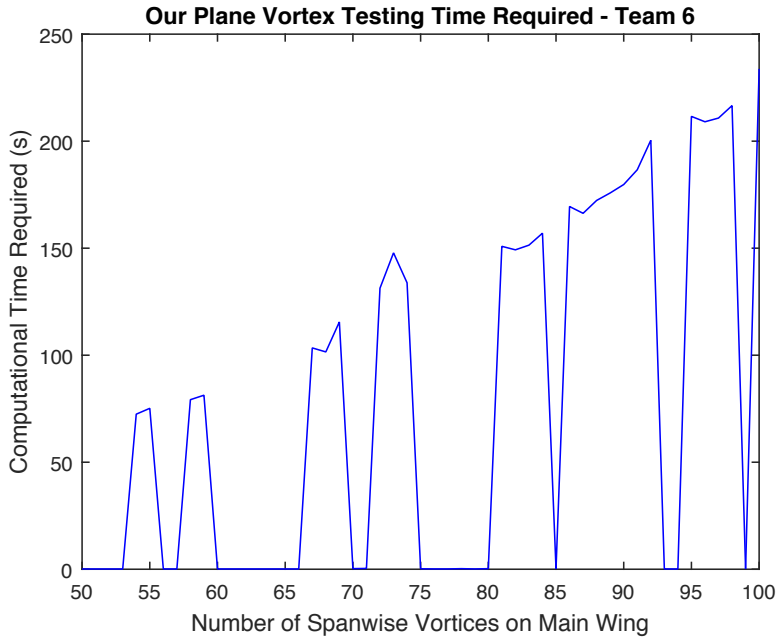

Figure 34: Computational time increases linearly with number of vortices, crashed runs are clearly visible from their near-zero computational time

sine, and cosine, bunching in the middle or near the ends. This means that if there is a flap end or a small section in a region near the middle where vortices are sparsely placed, AVL may not be able to put enough vortices in the sections where they are most needed. To determine the extent to which this method of section-by-section vortex distribution improved accuracy, we ran another

trade study using this method. We distributed the vortices among the eight sections of the wing, and varied the number of vortices in all sections by one at a time. The results show that there is no change in accuracy between 28 vortices and 60 vortices up to the ten-thousandths place, as can be seen in Figure 35. This was run at a different flight condition than the previous study, so the C_D is slightly different, but from the earlier study we knew that 60 vortices would be sufficient to ensure accuracy, so we see that 28 vortices distributed among the sections is also sufficient to ensure accuracy. As before, computational time increases linearly with number of vortices, as shown in Figure 36. The use of the distributed vortices reduced the required computational time significantly from roughly 70 seconds down to closer to 20. This saved significant time during our optimization, when AVL would be run hundreds of times, while also ensuring AVL would never crash. In the end, with our full fuselage and nacelles modeled as well as the lifting surfaces, AVL took an average of roughly 30 seconds to run.

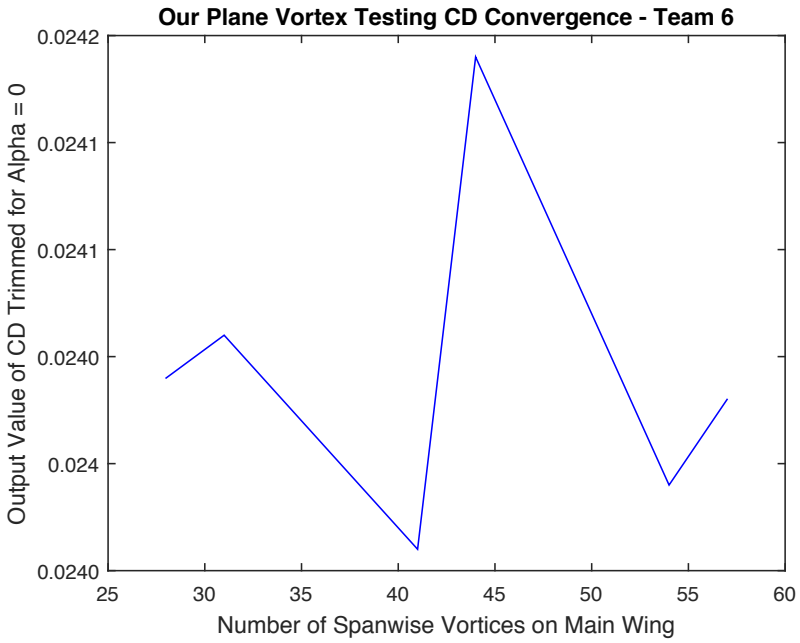

Figure 35: C_D remains nearly constant for all numbers of vortices if they are manually distributed among sections

B Airfoil Trade Study

An important part of our wing design was choosing an airfoil. This occurred very early in the design process. From the our early estimations, we had a general idea of what the cruise C_L would be, and thus we could look for the airfoil with the best performance at that C_L. The C_L we determined was 0.4855, and once this was know we could use the Korn equation to find the thickness of airfoil required to keep our drag divergence Mach number at least 0.02 above our cruise Mach number of 0.83. The thickness we determined, given as a fraction of the airfoil chord, was 0.1312, so we needed an airfoil that was less than roughly 13 percent thick. Knowing that supercritical airfoils typically give the best performance at transonic conditions such as our cruise condition, we focused on the supercritical airfoils available in the University of Illinois at Urbana-Champaign (UIUC) airfoil database, which consisted of the NASA Phase 2 airfoils, the Whitcomb supercritical airfoil,

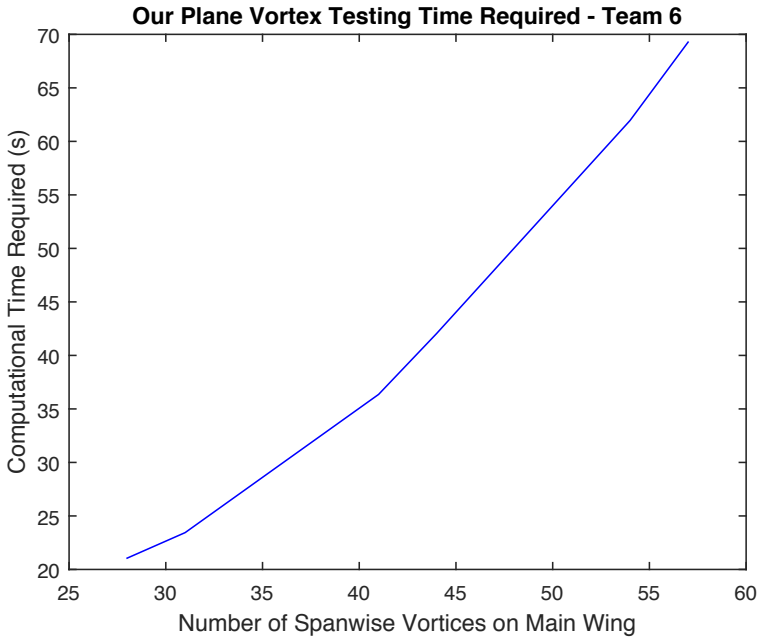

Figure 36: Computational time still increases linearly with number of vortices

and the Boeing 737 root, mid, and tip airfoils. The NASA Phase 2 airfoils are classified by design lift coefficient and maximum thickness as a percentage of chord. Thus, NASASC(2)-0714 denotes a NASA phase 2 supercritical airfoil with a design C_l of 0.7 and a maximum thickness of 14 percent chord. The airfoils available on the UIUC database included those with design C_L's of 0.0, 0.4, 0.5, 0.6, 0.7, and 1.0, along with the 737 airfoils, which appeared more symmetrical than most of the supercritical airfoils, indicating lower design C_l's. We ran these airfoils through XFoil at our estimated cruise C_L of 0.4855, preliminary perpendicular Mach number of 0.719, and a Reynolds number of 36×10^6 based on our cruise speed, cruise altitude, and preliminary root chord, with the goal of finding the airfoil with the highest L/D at that cruise condition. We used the exact cruise C_L, without any correction to convert it to a sectional C_l more appropriate for 2-dimensional airfoil analysis, because we expected changes anyway as the design was refined and the wing-loading and wing area changed, so we assumed the airfoil that had the highest L/D at a C_l of 0.4855 would also have the highest L/D at whichever nearby C_l ended up being used in our final design. XFoil required a fair amount of finesse to be coaxed into convergence at these high Mach numbers, but we were able to get results for 23 airfoils at our cruise perpendicular Mach number of 0.719, given our preliminary sweep of 30.5°. Considering our known constraint on thickness and goal of highest L/D at cruise, we used a plot of cruise L/D as a function of thickness to compare the airfoils. The SC(2) airfoils of the same design C_l were connected by lines, as were the 737 airfoils to allow for easier comparison. This plot can be seen in Figure 37.

Contrary to our expectation, for a given thickness the L/D decreased monotonically as design C_L increased, which meant the more symmetric airfoils had the highest L/Ds. We expected the SC(2)-05XX airfoils to perform the best at the C_L of 0.4855, very close to 0.5. However, the 737 airfoils, the most symmetrical-looking of them all, had the highest L/D. This wasnt entirely unexpected because Boeing presumably designed high-performance airfoils for the 737. However, as a simple check of our results, we ran a NACA 2412 airfoil, and surprisingly, it outperformed all previous airfoils, giving an L/D of 93.41, compared to the 737 mid-wing airfoils 86.75, the previous

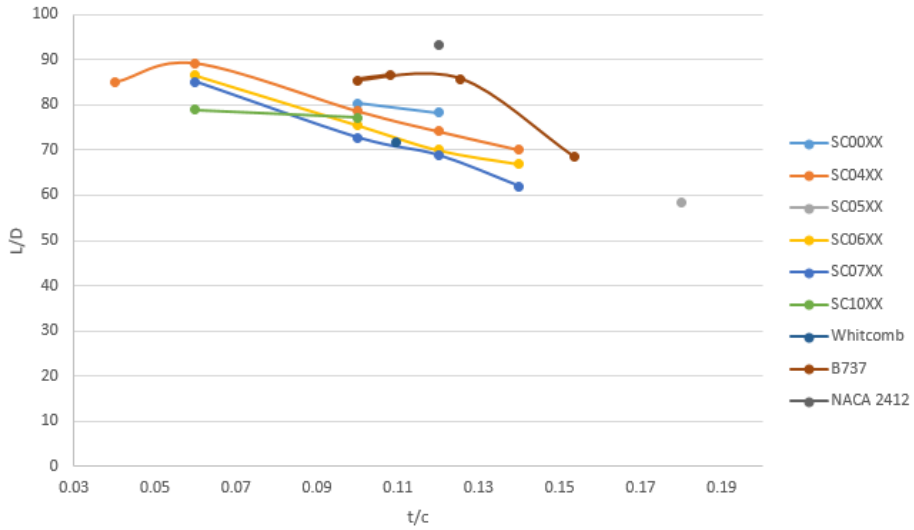

Figure 37: L/D at cruise condition as a function of t/c

best in our thickness range. This led us to question the validity of our XFoil results. We suspect that the Mach numbers at which we were testing were too high for XFoil to give accurate results. Regardless of the cause of the inaccuracy, however, we were in need of more reliable data on which to base an important design decision.

To gain a better insight into the options for transport aircraft airfoils, we researched the development of supercritical airfoils. According to Harris [12], the first generation of supercritical airfoils designed by NASA in the early- to mid-1960s anticipated high-speed transport aircraft and thus had a design C_l of 0.7. However, later design studies suggested a need for lower cruise Mach numbers than expected and thus the design C_l was changed to roughly 0.55, and the elimination of drag creep at Mach numbers close to the drag divergence Mach number was made a design goal. Later, the phase 2 supercritical airfoils were designed to have a range of cruise lift coefficients, but while wind tunnel data was taken on all earlier airfoils, only phase 2 airfoil 0714 has published wind tunnel data, and its design C_l of 0.7 led to inferior performance in our operating range around 0.5, as can be seen in Figure 38 and Figure 39.

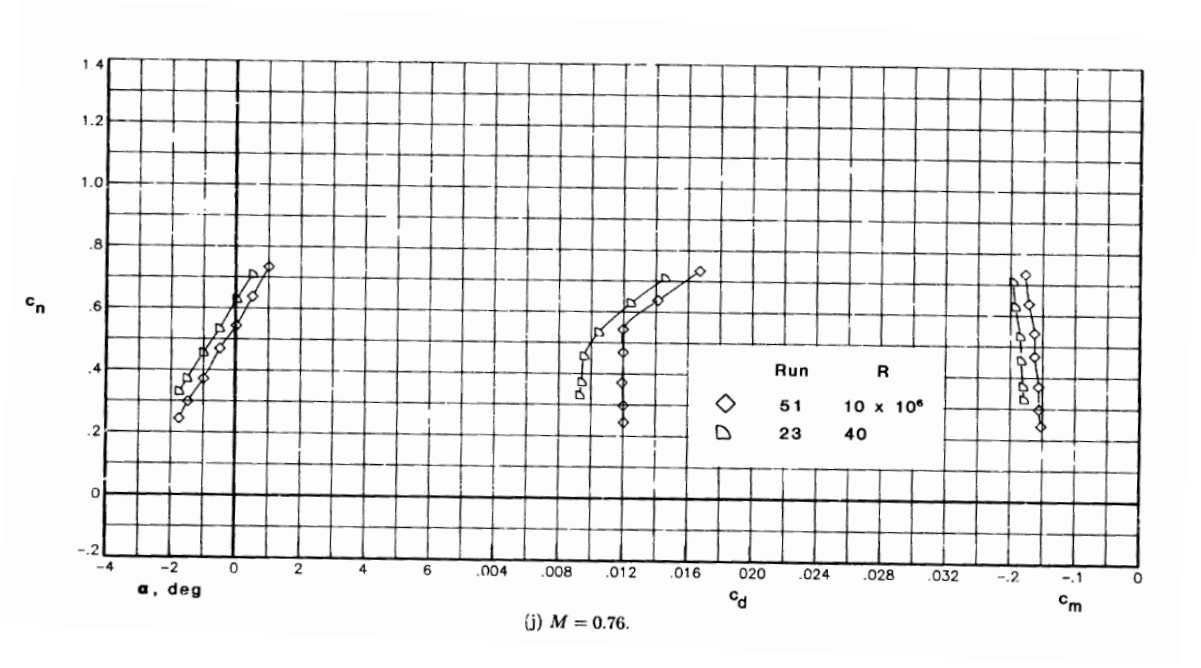

Figure 38: Wind tunnel data showing the performance of SC(2)-0714 at various normal force coefficients at a Mach number of 0.76 (*as presented in* [13])

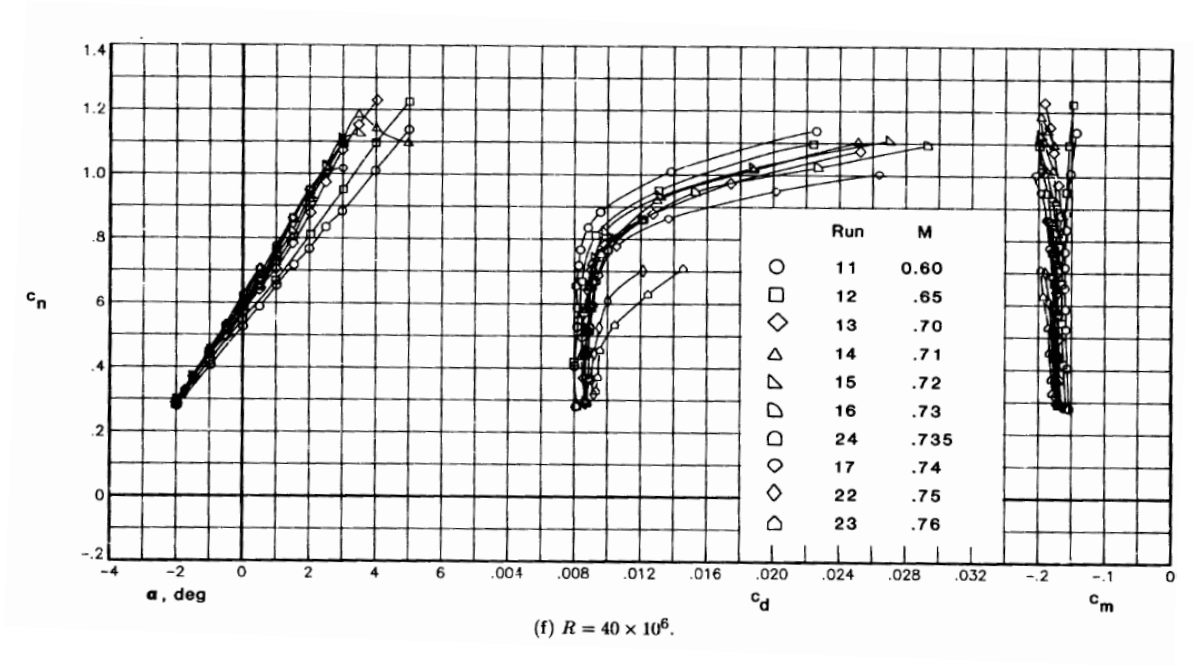

Figure 39: Wind tunnel data showing the performance of SC(2)-0714 at various normal force coefficients at a Reynold's number of 40 million (*as presented in* [13])

Thus, our focus was on the airfoils designed for a C_l of 0.55, near our estimated 0.4855 cruise C_L. This difference was ideal, because the wing C_L will be lower than the sectional C_l, so if the sectional C_l is designed to be 0.55, the wing C_L may be around our 0.4855. The two airfoils with our

desired design C_l that have published wind tunnel data are airfoil 26a, which was experimentally designed by NASA and an airfoil theoretically designed by P. Garabedian of New York University using the complex hodograph method. Both were tested in NASAs Langley 8-foot transonic wind tunnel, and the results are shown in figs. 40 to 42.

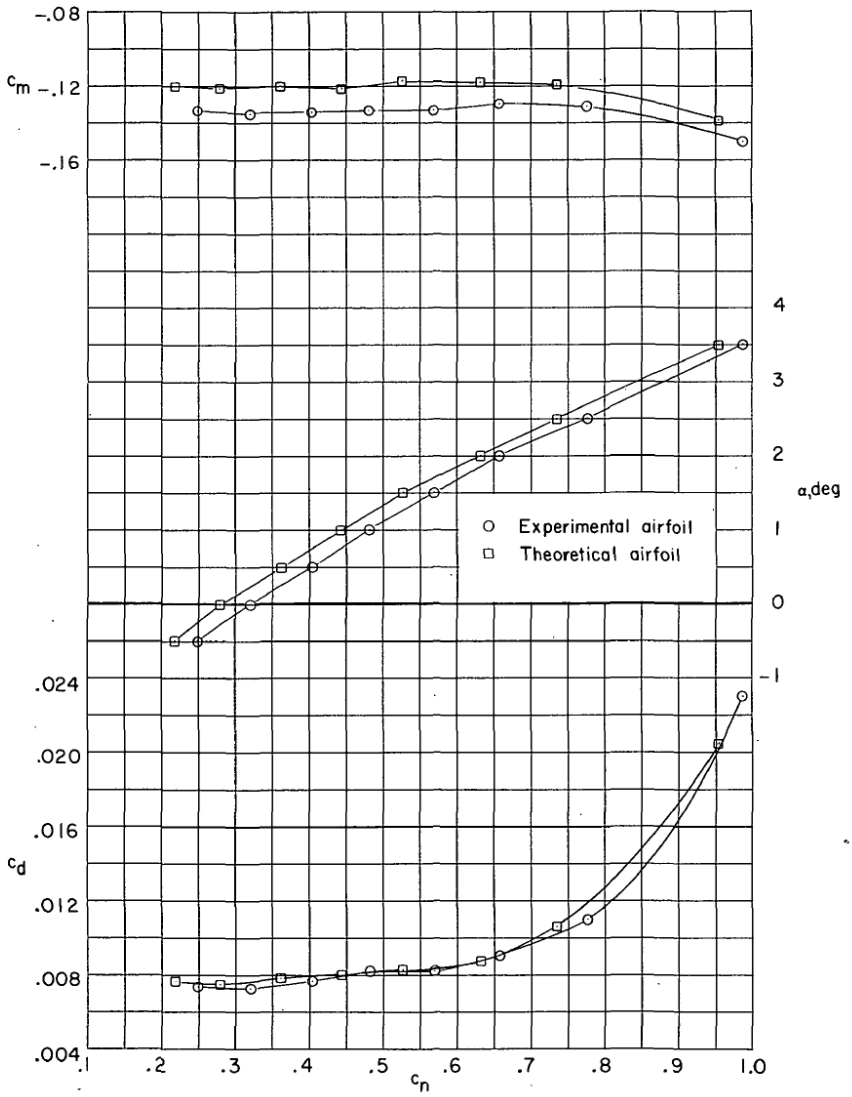

Figure 40: Wind tunnel data showing the performance of airfoil 26a and the theoretically designed airfoil at various normal force coefficients at a Mach number of 0.76 (*as presented in* [14])

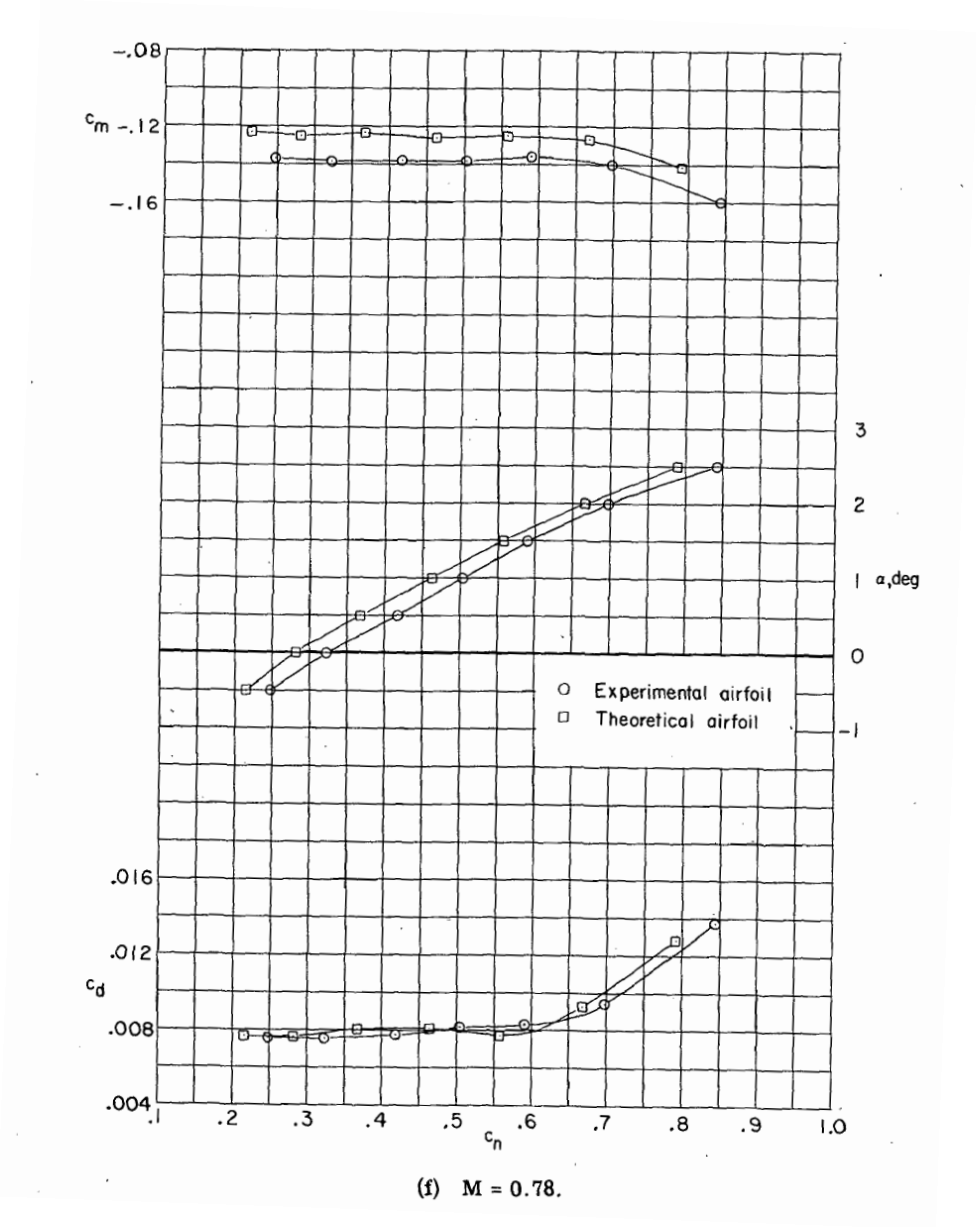

Figure 41: Wind tunnel data showing the performance of airfoil 26a and the theoretically designed airfoil at various normal force coefficients at a Mach number of 0.78 (*as presented in* [14])

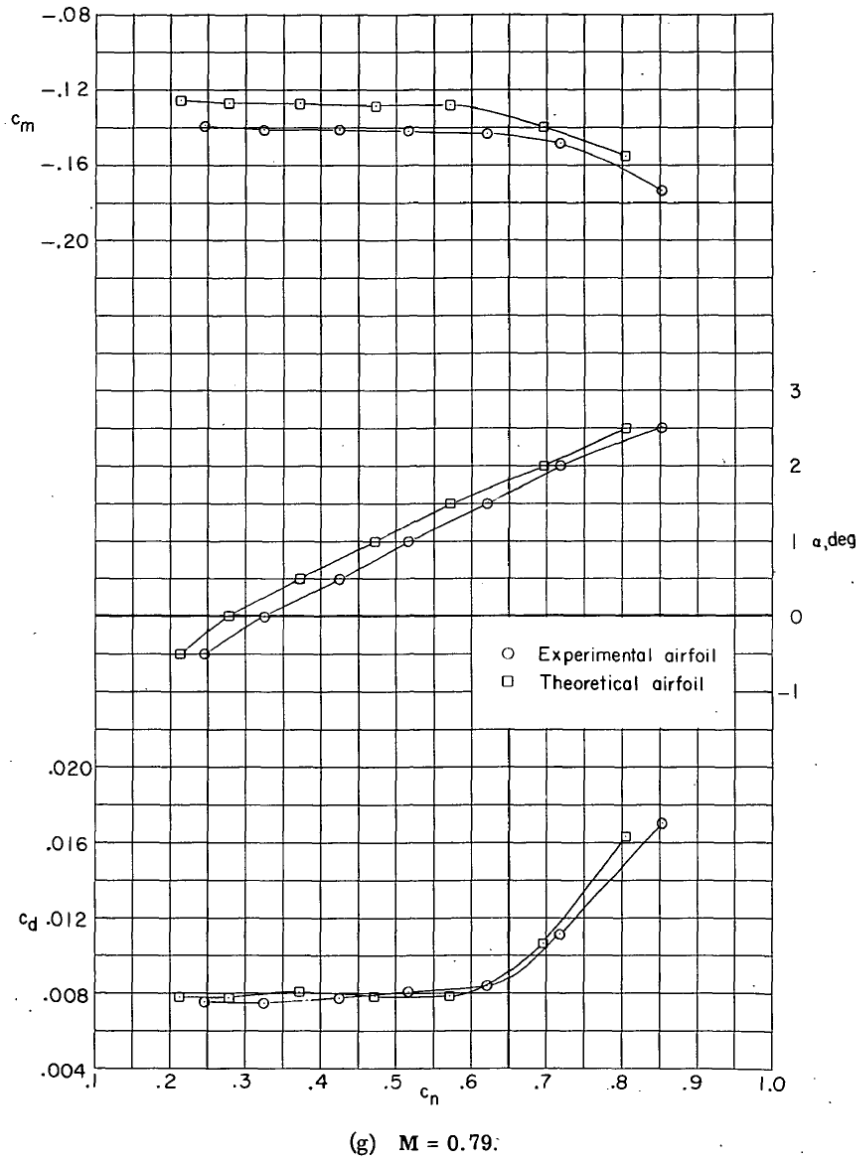

Figure 42: Wind tunnel data showing the performance of airfoil 26a and the theoretically designed airfoil at various normal force coefficients at a Mach number of 0.79 (*as presented in* [14])

Airfoil 26a has a design C_l of 0.55, and the shockless airfoil has a design C_l of 0.59 and a design Mach number of 0.78. At this condition the shockless airfoil uses compression waves reflected off the sonic line between the supersonic flow on the upper surface of the airfoil and the surrounding subsonic flow to recompress the flow prior to the shock farther aft. These waves are present on all supercritical airfoils, and compress the flow isentropically to maintain the region of roughly constant pressure on the upper surface while reducing the drag caused by the shock at the aft end of the supersonic region. Garabedians airfoil is tuned such that there is no shock at all at the design condition. Harris emphasizes that this design has degraded off-design performance because of its focus on completely eliminating the shock, whereas airfoil 26a was designed to have minimal wave drag over a range of conditions. Considering that 3-D effects will make the C_L of the wing lower than the sectional C_l of the airfoil, we compared the airfoils at a C_l of 0.6, which gives a 0.1

margin from our estimated cruise C_L of 0.4855. The theoretically designed airfoil has higher L/Ds than airfoil 26a in the range of conditions around our cruise condition, even at points away from its design point, as can be seen in the comparisons of the two airfoils performance in Figure 40. Based on this data, we chose the shockless airfoil to achieve the largest L/D possible for our main wing at cruise.

Comparing performance in the vicinity of this C_l, we noticed that both airfoils have a drag divergence Mach number of roughly 0.80. This was confirmed by figs. 43 and 44, shown below.

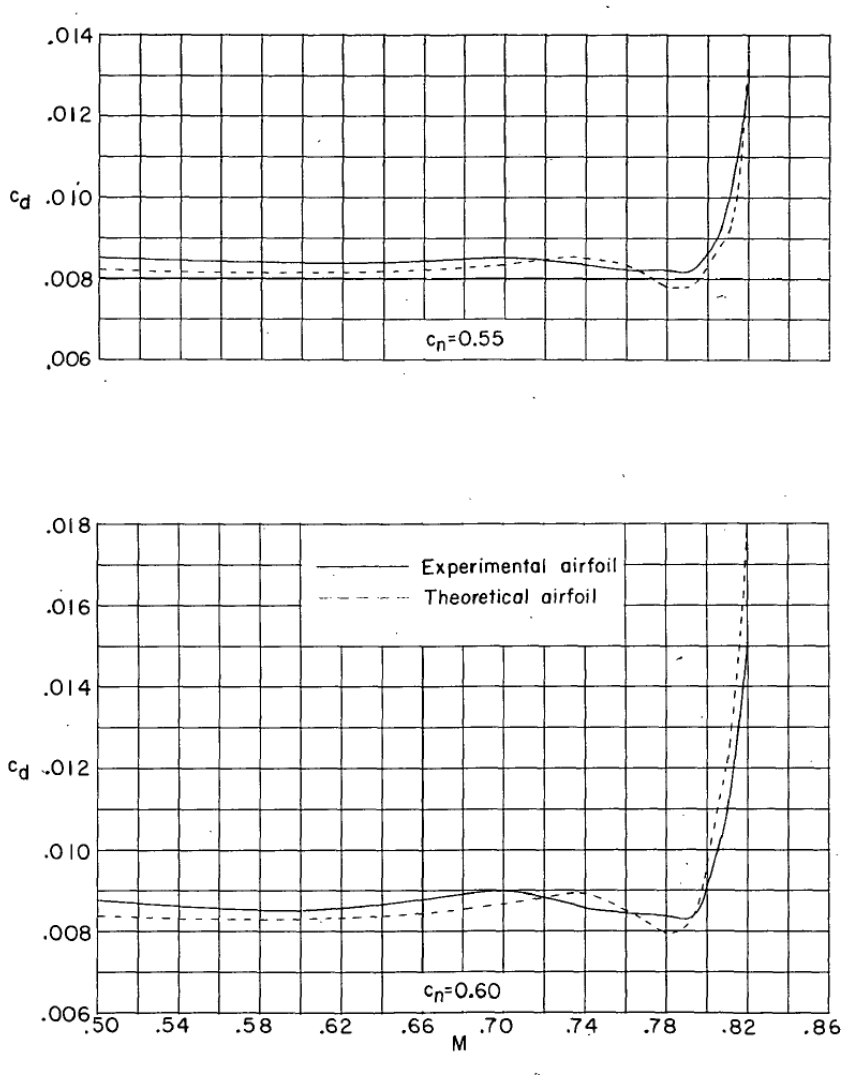

Figure 43: Wind tunnel data showing the performance of airfoil 26a and the theoretically designed airfoil at Mach numbers at normal force ceofficients of 0.55 and 0.6 (*as presented in* [14])

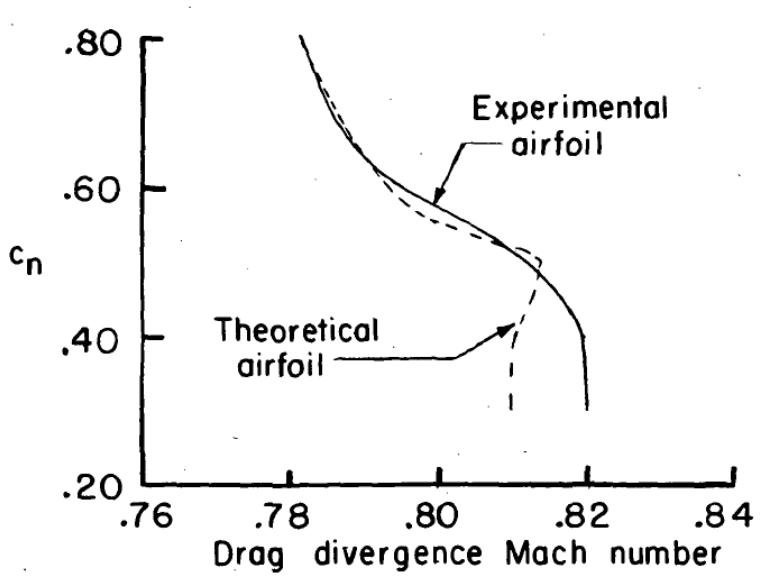

Figure 44: Wind tunnel data showing the drag divergence mach number of the two airfoils as a function of normal force coefficient (*as presented in* [14])

This is significantly higher than we expected given the sweep angles and cruise Mach numbers of similar aircraft. According to the slides, the drag divergence Mach number should be 0.02 greater than the cruise Mach number to avoid wave drag. Thus, if our airfoils drag divergence Mach number is 0.80, we only need to sweep the wings enough to reduce the cruise perpendicular Mach number seen by the airfoil to 0.78. However, in addition to decreasing the C_L, 3-D effects will also accelerate the onset of compressibility effects, so we doubled the 0.02 margin from the notes, and arrived at a cruise perpendicular Mach number of 0.76. This allowed us to reduce our sweep angle from the 30.5° based on historical data to 23.7°. A lower sweep angle is desirable because it gives a longer span for a given wing weight. Span is measured perpendicular to the fuselage, so in order to get the same span at a higher sweep angle, more wing is required, but that will add weight. The span is set by the aspect ratio, which is important for reducing induced drag, so meeting our set span is important to achieving our performance goals. Thus a less-swept wing allows us to save weight for a given span, as was confirmed by our optimization.

References

[1] European Aviation Safety Agency, *General Electric Company, GEnx Series Engines*, No. TCDS IM.E.102, January 2014.

[2] European Aviation Safety Agency, *GE Aircraft Engines, GE90 Series Engines*, No. TCDS IM.E.002, March 2004.

[3] European Aviation Safety Agency, *Rolls-Royce RB211 Trent 900 Series Engines*, No. TCDS E.012, December 2013.

[4] European Aviation Safety Agency, *International Aero Engines, LLC, PW1100G-JM Series Engines*, No. TCDS IM.E.093, October 2015.

[5] Roskam, J., *Various titles*, Vol. 1-8 of *Airplane Design*, DARcorporation, 2002.

[6] Martins, J. R. R. A., "Aircraft Design," Supplementary notes for AE481 course at the University of Michigan, 2015.

[7] Kroo, I. M., "Aircraft Design: Synthesis and Analysis," .

[8] Raymer, D. P., *Aircraft Design: A Conceptual Approach*, AIAA, 2006.

[9] Daniel P. Raymer, J. W., "Advanced Technology Subsonic Transport Study," Technical Memorandum NASA TM 2011-217130, NASA Glenn Research Center, November 2011.

[10] A.B. Lambe, J. M., "Extensions to the Design Structure Matrix for the Description of Multidisciplinary Design, Analysis, and Optimization Processes," *Structural and Multidisciplinary Optimization*, Vol. 46, No. 2, 2012, pp. 237–284.

[11] Drela, M. and Youngren, H., *Athena Vortex Lattice (AVL)*, MIT Aero & Astro, 3rd ed., February 2014.

[12] Harris, C. D., "NASA Supercritical Airfoils: A Matrix of Family-Related Airfoils," Technical Paper NASA TP-2969, NASA Langley Research Center, March 1990.

[13] Renaldo V. Jenkins, Acquilla S. Hill, E. J. R., "Aerodynamic Performance and Pressure Distributions for a NASA SC(2)-0714 Airfoil Tested in the Langley 0.3-Meter Transonic Cryogenic Tunnel," Technical Memorandum NASA TM-4044, NASA Langley Research Center, July 1988.

[14] Harris, C. D., "Comparison of the Experimental Aerodynamic Characteristics of Theoretically and Experimentally Designed Supercritical Airfoils," Technical Memorandum NASA TM X-3082, NASA Langley Research Center, July 1974.